5361_02

Resonance scattering of Fe XVII X-ray and EUV lines

A. K. Bhatia
Laboratory for Astronomy and Solar Physics
NASA/Goddard Space Flight Center
Greenbelt, Maryland 20771

and

J. L. R. Saba
Lockheed Martin Solar and Astrophysics Laboratory at NASA
Greenbelt, Maryland 20771

Abstract

Over the years a number of calculations have been carried out to derive intensities of various X-ray and EUV lines in Fe XVII to compare with observed spectra. The predicted intensities have not agreed with solar observations, particularly for the line at 15.02 Å; resonance scattering has been suggested as the source for much of the disagreement. The atomic data calculated earlier used seven configurations having n=3 orbitals and the scattering calculations were carried out only for incident energies above the threshold of the highest fine-structure level (Bhatia & Doschek 1992). These calculations have now been extended to thirteen configurations having n=4 orbitals and the scattering calculations are carried out below as well as above the threshold of the highest fine-structure level. These improved calculations of Fe XVII change the intensity ratios compared to those obtained earlier, bringing the optically thin F(15.02)/F(16.78) ratio and several other ratios closer to the observed values. However, some disagreement with the solar observations still persists, even though the agreement of the presently calculated optically thin F(15.02)/F(15.26) ratio with the experimental results of Brown et al. (1998) and Laming et al. (2000) has improved. Some of the remaining discrepancy is still thought to be the effect of opacity, which is consistent with expected physical conditions for solar sources. EUV intensity ratios are also calculated and compared with observations. Level populations and intensity ratios are calculated, as a function of column density of Fe XVII, in the slab and cylindrical geometries. As found previously, the predicted intensities for the resonance lines at 15.02 and 15.26 Å exhibit initial increases in flux relative to the forbidden line at 17.10 Å and the resonance line at 16.78 Å as optical thickness increases. The same behavior is predicted for the lines at 12.262 and 12.122 Å. Predicted intensities for some of the allowed EUV lines are also affected by opacity.

1. INTRODUCTION

Neon-like Fe XVII is present in solar flares and active regions in a broad temperature range (2-10) $\times 10^6$ K because of the filled 2p shell. Strong resonance lines in the range 15-17 Å have been observed from the Sun with early sounding rockets (e.g., Blake et al. 1965 and Hutcheon, Pye, & Evans 1976) and subsequently with satellites (e.g., Rugge & McKenzie 1985 and Phillips et al. 1982). The transitions of primary interest are $2s^22p^53d\ ^1P_1 \rightarrow 2s^22p^6\ ^1S_0$ at 15.02 Å and $2s^22p^53d\ ^3D_1 \rightarrow 2s^22p^6\ ^1S_0$ at 15.26 Å. Other lines of particular interest are those at 15.45, 16.78, 17.05, 17.10 Å, along with subordinate lines in the extreme-ultraviolet (EUV) region.

More recently, a number of Fe XVII lines have been observed from astrophysical sources in the spectra obtained from the Chandra X-ray observatory: Kaastra et al. (2000) observed absorption lines at 12.274, 13.826, 15.014, and 15.265 Å in the spectrum of the Seyfert 1 galaxy NGC 5548. Kaspi et al. (2000) observed absorption lines at 11.250 and 15.264 Å in the spectrum of the Seyfert 1 galaxy NGC 3783. Using the Low-Energy Transmission Grating Spectrometer, Brinkman et al. (2000) observed twenty three lines at 13.82, 15.02, 15.27, 15.46, 16.30, 16.78, 17.05, 17.10, 30.02, 34.10, 34.20, 36.40, 51.15, 51.27, 60.04, 68.20, 68.40, 75.06, 85.24, 85.44, 90.08, 102.30, and 102.57 Å in the spectrum of Capella, a binary system with a period of 104 days. Canizares et al. (2000) report line fluxes from lines at 15.013, 15.272, 16.796, 17.071, and 17.119 Å from Capella using the High-Energy Transmission Grating Spectrometer. The high resolution spectrum of ζ Puppis obtained with the XMM-Newton shows lines at 15.01, 15.26, 16.78, 17.05, and 17.10 Å, although the emitting plasma is not expected to be in thermal equilbrium, due to the presence of shocks and an intense ultraviolet radiation field (Kahn et al. 2000).

There have been a number of theoretical studies of the expected spectrum assuming optically thin conditions. Bhatia & Doschek (1992, hereinafter BD) carried out a distorted wave calculation using seven configurations, $2s^22p^6$, $2s^22p^53s$, $2s^22p^53p$, $2s^22p^53d$, $2s2p^63s$, $2s2p^63p$, and $2s2p^63d$, giving rise to 37 fine-structure levels. Collision strengths were calculated at five incident energies. Their collision strengths are in good agreement with those of Zhang et al. (1987), Zhang & Sampson (1989), and Hagelstein & Jung (1987). The level populations and intensity ratios were calculated as a function of electron density and temperature.

The Fe XVII level structure is distinguished in having all the excited levels much higher than the single ground level $^1S_0$, implying that even at high electron densities most of the ion population is in the ground level. The EUV lines have been observed in solar flare spectra recorded by a Naval Research Laboratory slitless spectrograph flown on the Skylab manned space station in 1973 (Feldman et al. 1985; Doschek, Feldman, & Bhatia 1991). The predicted relative intensities of these lines at $N_e=10^{11}cm^{-3}$ and $T_e=4\times10^6$K agree fairly well with the observed relative intensities, which are accurate to within 30%, except for the line at 409.69 Å which disagrees by a factor of two.

For optically thin plasma, the ratio F(15.02)/F(15.26) according to the previous (BD) calculation is 4.1, while the typical observed solar ratios are 2.75 ± 0.7 for flares (McKenzie et al. 1980; Phillips et al. 1982) and 2.1 ± 0.3 for active regions (see Table 14); the experimental value of Brown et al. (1998) using the Electron Beam Ion Trap (EBIT) at Lawrence Livermore National Laboratory (LLNL) is 3.04 ± 0.12. Comparing with the EBIT ratio, Brinkman et al. (2000) concluded that there is little or no evidence for opacity effects in the line at 15.014 Å seen in the Capella spectrum.

The observed intensity ratios of various Fe XVII soft X-ray lines from solar active regions do not agree with the optically thin calculated intensity ratios and it was suggested by Rugge & McKenzie (1985) that these lines suffer resonance scattering. Resonance scattering implies that the emitted photon is absorbed and reemitted but not necessarily in the line of sight, so there can be an apparent loss or enhancement of flux although the total flux integrated over 4π remains unchanged.

The simplest way to take into account optical depth effects is to multiply the transition rates by constant escape probabilities. Various approximate treatments, e.g., Phillips et al. (1996) and Saba et al. (1999), have been carried out to interpret observations of the disk center to limb intensity variation. Saba et al. (1999) used the escape probability method of Kastner & Kastner (1990) and concluded that the intensity of the 15.02 Å line was a factor of 2 to 3 lower than the predicted optically thin value.

2. NEW CALCULATION OF THE OPTICALLY THIN SPECTRUM

These inferences are based on the atomic data calculated by BD, who carried out the scattering calculations for five incident energies chosen to be above the threshold of the highest fine-structure level. This restriction was due to the limitation of the JJOM program of Saraph (1978) which has now been improved by Saraph & Eissner (2001) such that collision strengths can now be calculated below the threshold as well.

To improve the target representation, these calculations have been repeated by adding six more configurations having n=4 orbitals, namely $2s^22p^54s$, $2s^22p^54p$, $2s^22p^54d$, $2s2p^64s$, $2s2p^64p$, and $2s2p^64d$, giving rise to 73 fine-structure levels. The structure calculations have been carried out using the Superstructure program developed by Eissner et al. (1972), which includes relativistic corrections. Collision strengths are calculated at eleven incident energies: four below the threshold energy of 84.066 Ry and seven above. The incident energies below the threshold are 55.8, 65, 70, and 76 Ry and those above are 85, 127.5, 170, 212.5, 255, 340, and 425 Ry. The collision strengths are calculated up to total angular momentum $L^T = 33$:

$$\vec{L^T} = \vec{l_i} + \vec{l_t}, \tag{1}$$

where $\vec{l_i}$ is the incident angular momentum and $\vec{l_t}$ is the target angular momentum. The newly calculated atomic data for the transitions of interest in the X-ray and EUV regions will be published elsewhere in their entirety (Bhatia & Doschek 2001), but are discussed here briefly. In Table 1, a comparison of the presently calculated energies of the lowest 37 levels with the results of the previous 37-level calculations and observations shows improvement in the energy values of the levels. In Table 2, the calculated energies of levels arising from n=4 configurations are given along with the values inferred from observed wavelengths of Phillips et al. (1982) and calculated values from the National Institute of Standards and Technology (NIST) compilation (Sugar and Corliss 1985).

Table 3 compares oscillator strengths and radiative rates for a few transitions obtained from the 73-level (13 configuration) calculation with those from the 37-level (7 configuration) calculation. Collision strengths for electron impact excitation for a few transitions of interest are given in Table 4. A comparison of the new collision strengths with the previous results for the $1 \rightarrow 5$ transition is given in Figure 1: there is good agreement at low incident energies with some deviations at high incident electron enegies. This is understandable because the present calculation includes many more incident partial waves in the scattering calculation.

Using the presently calculated atomic data for 73 levels, Table 5 gives intensity ratios (in photon units, relative to the 16.78 Å line) for the lines at 15.02, 15.26, 15.45, 16.34, 17.05, and 17.10 Å, for $N_e = 10^{11} cm^{-3}$ and $T_e = 4 \times 10^6 K$, the temperature of maximum abundance of Fe XVII (Arnaud & Raymond 1992). The ratios are given with respect to the 16.78 Å line because this line is chosen as the reference line by many observers. This table shows results from the models consisting of 27, 37, 63, and 73 levels derived from the present calculation. Also shown for comparison are the values for the previous model of BD with 37 levels. The line ratios seem to converge as the number of levels is increased in the present model. It is not possible to predict how the ratios would change when configurations with n=5 and 6 orbitals are added but some estimates have been made for a few transitions by Liedahl (2000), who indicates an asymptotic convergence when n=5 and 6 orbitals are added.

We find that the ratio F(15.02)/F(15.26) is equal to 3.7 for the 73-level model compared to the previous value of 4.1 for this ratio (BD); that is, it has moved 10% closer to the experimental ratio (Brown et al. 1998) of 3.04 ± 0.12.

In Table 6, the intensity ratios are given at various electron densities for $T_e = 4 \times 10^6 K$. We find the variation with density is not very significant for $10^8 \leq N_e \leq 10^{12}$; we take $N_e = 10^{11} cm^{-3}$ (an electron density intermediate between coronal values expected for active regions and for flares) as an appropriate electron density for most of our analysis. The variation with respect to the electron temperature is indicated in Table 7 for the range of temperatures corresponding to active regions (2-6$\times 10^6$K). Some of these line ratios, for example F(15.45)/F(15.26), might be useful temperature diagnostics in the optically thin regime (although the 15.45 Å line is fairly weak). For most of our analysis here, we use $T_e = 4 \times 10^6$K, the temperature of the maximum abundance of Fe XVII.

We also present in Tables 8A and 8B, for $T_e = 10^6$ and 10^7K respectively, the intensity variation with respect to electron density of all the X-ray lines found in the range 11 to 18 Å in this calculation. (Weak lines corresponding to relative intensities less than 10^{-5} of the brightest line are omitted.) These should be useful to compare with new observations from the XMM-Newton and Chandra satellites.

In Table 9, we give intensity ratios of the EUV lines with respect to the dipole-forbidden line at 17.10 Å and compare them with the results of Bhatia and Kastner (1999, hereinafter BK) obtained with the 37-level model. Some variations are noticed. But the present ratio of 1.5 for F(350.5)/F(347.85) does not change significantly compared to the ratio obtained from the previous calculation, while that observed from the Solar EUV Rocket Telescope and Spectrograph (SERTS) is 1.9 ±1.0 (Brosius et al. 1996) and 1.5 ± 0.5 (Thomas & Neupert 1994).

3. THE OPTICALLY THICK SPECTRUM

We simulate the optically thick equilibrium situation by following the procedure of BK in which the multiplying factors are escape factors appropriate to the chosen geometry, which are functions of optical thickness and therefore also of level populations. The resulting nonlinear system of equations is solved by iteration, starting from the optically thin level populations as the initial population vector. Two geometries, plane-parallel (slab) geometry and cylindrical geometry are again considered. The cylindrical geometry resembles more the geometry of radiating solar filaments in active regions. The Doppler-profile escape factors for both geometries are given in BK and are repeated here briefly. The Doppler-profile escape factor for the slab geometry has been given by Capriotti (1965) (we define our τ as his $2\tau^c$) as

$$SEF(\tau) = 1 - (0.8293)\tau^c + (0.7071)\tau^c ln(2\tau^c) + \sum_{k=1}^{\infty} \frac{(-1)^k (\tau^c)^{2k+1}}{k(k+2)!(k+2)^{1/2}} \quad (2)$$

for $\tau^c \leq 2.5$, and

$$SEF(\tau) = \frac{([ln(2\tau^c)]^{1/2} + 0.25[ln(2\tau^c)]^{-1/2} + 0.14)}{(2\sqrt{\pi}\tau^c)} \quad (3)$$

for $\tau^c > 2.5$.

The optical thickness at the line center is given by

$$\tau = 1.161 \times 10^{-14} f \lambda(\AA) \sqrt{\frac{M}{T_D}} (N_1 L) \tag{4}$$

where f is the oscillator strength, $N_1(cm^{-3})$ the population of the ground state, L(cm) the path length, M the atomic mass number and T_D is the Doppler temperature. It should be noted that τ is a function of the ion temperature T_D which is taken here to be the same as T_e.

For cylindrical geometry, values of the Doppler-profile escape factor CEF(τ) have been calculated by Bhatia and Kastner (1997, hereinafter BK97) and expressed as the logistic function

$$CEF(\tau) = \frac{1}{1 + exp[b(log\tau - c)]} \tag{5}$$

where b=2.2952969 and c=0.046747185.

From the observer's point of view, the emergent intensities contain also as factors the monodirectional escape probabilities $p_f(D, k, \tau_0, 1)$, which have been discussed for slab and cylindrical geometries by Kastner & Kastner (1990) and BK97.

The monodirectional single-flight or free-flight photon escape probability, assuming a constant source function, is given by Kastner & Kastner (1990) as

$$p_f(D, \tau; 1) = (\sqrt{\pi}\tau)^{-1} \int_{-\infty}^{\infty} (1 - \exp[-\tau \exp(-x^2)])dx \tag{6}$$

where the dimensionless frequency variable $x = (\nu - \nu_0)/\Delta\nu_D$. The escape probability, expressed as a logistic function, is given by

$$p_f(D, \tau; 1) = \frac{1}{1 + \exp(b[log(\tau) - c])} \tag{7}$$

where b=2.410527 and c=0.3950445 for the slab geometry and b=2.3212136 and c=0.22335545 in the cylindrical geometry. The present analysis is strictly valid for lines which are not self-reversed, i.e., for $0 < \tau < 15$. In general, for $\tau > 15$, self-reversal is expected for some lines. In this particular case, for column density approaching $10^{18} cm^{-2}$ or so (with $\tau > 100$ for the 15.02 Å line), there is still no obvious problem in solving these statistical equilibrium equations.

The emergent intensity for an optically thick plasma is given by

$$I_{ji} = N_j A_{ji} p_f(D, \tau; 1) = I_{ji}(\text{optically thin}) \mathrm{p_f(D}, \tau; 1) \tag{8}$$

Solutions of the statistical equations were carried out for the slab and cylindrical geometries at the electron temperature $T_e = 4 \times 10^6$ K and for three electron density values $N_e = 10^9$, 10^{11}, and $10^{13} cm^{-3}$. For each case, assumed Fe XVII column densities ranged from 0 (optically thin) to at least $10^{21} cm^{-2}$. Convergence from the initial optically thin population vector to the equilibrium solution was rapid, usually within four iterations.

We find that the upper level populations of the reference lines 17.10 and 254.87 Å do not increase or decrease with increasing column length. However, the upper level population of the most optically thick resonance line at 15.02 Å increases dramatically with increasing column length, as indicated in Figure 2 for the cylindrical geometry. A similar but more extreme behavior is found for the slab geometry. The total increase is seen to be a factor of about 10^3, reaching a saturation at column densities greater than about $10^{20} cm^{-2}$, after which the level populations are independent of column density.

The calculated photon fluxes, as a function of column density, of the six resonance lines at 17.05, 16.78, 15.45, 15.26, 15.02, and 13.82 Å are given for active region conditions in Tables 10 (slab geometry) and 11 (cylindrical geometry), relative to the forbidden line at 17.10 Å. The behavior of these resonance lines relative to the 17.10 Å forbidden line is shown in Figure 3 for cylindrical geometry. The dependences on column density of the relative fluxes of the resonance lines at 15.02, 15.26, and 15.45 Å with respect to the 16.78 Å line are given in Figure 4, along with the corresponding values of τ for each line depicted.

As pointed out earlier by BK, all the resonance lines show an initial increase in flux relative to the forbidden line, as column density increases. This behavior is contrary to the common expectation that resonance lines monotonically decrease in intensity with opacity relative to forbidden line intensities. This expectation is based on the erroneous assumption that at low opacities level populations are independent of opacity and that more resonance line photons are scattered out of the line of sight than are scattered into it (Doyle and McWhirter 1980). On the contrary, as illustrated in Figure 2 for the $2p^5 3d(^1P_1)$ level, level populations do depend on opacity, which in turn makes the escape factors depend upon level populations nonlinearly; this is the source of the initial increase with the increase of column density of the fluxes of the resonance lines relative to the 17.10 Å line shown in Figure 3, and the more complicated behavior of the 15.02 and 15.26 Å lines with respect to 16.78 Å line, as shown in Figure 4.

We find that the X-ray lines at 12.670, 12.522, 12.321, 12.261, 12.122, 11.042, 11.023, and 10.840 Å, originating from n=4 configurations, are also optically thick. In particular the predicted intensities for the lines at 12.262 and 12.122 Å, show an initial increase in flux relative to the forbidden line at 17.10 Å as column density increases. Early observations of these lines were reported by Walker, Rugge, & Weiss (1974) and Hutcheon, Pye, & Evans 1976; the lines were also seen by the SMM satellite (Phillips et al. 1982), although their relative intensities were not discussed because of rapid changes in intensity due to the flare in progress.

Table 12 lists the calculated photon fluxes of the allowed $3d \rightarrow 3p$ EUV lines relative to the flux of the reference line at 254.9 Å. These lines are affected significantly by optical thickness because their upper levels are directly or indirectly pumped by the resonance line radiation field, especially the lines at 193.7, 226.1, 240.4, and 324.5 Å, which are affected most by opacity because their upper level is that of the strongest line at 15.02 Å.

Table 13 lists the calculated flux of the EUV lines relative to the flux of the line at 17.10 Å. These lines are unaffected by opacity and therefore the ratio F(350.5)/F(347.85) remains unchanged with increasing column length.

4. X-RAY OBSERVATIONS

4.1 *15.02/15.26 Ratio*

Many of the available solar measurements of the Fe XVII 15.02/15.26 ratio are summarized in Table 14. The entries include some older observations and cover a wide range in size of instrument field of view (FOV) and spectral resolution. Where pointing information was readily available, the values for limb regions (here taken to be those with θ, the angular distance from disk center, $\geq 85°$) are given separately from disk regions. For a given size FOV, there appears to be a small systematic disk/limb difference in the data, in the sense that the 15.02/15.26 ratio is slightly lower at the limb. This is in marked contrast to the values reported by Phillips et al. (1997), which show a strong increasing trend from center to limb; from tabulated values for nonflaring active regions in their Table 5, we obtain a mean value of 1.97 ± 0.14 for (32) disk ratios and 2.77 ± 0.22 for (11) limb ratios, where the quoted sigmas reflect the variance. Phillips et al. (1996) reported the same behavior, namely, a disk-to-limb increase, for the 15.01/16.78 ratio. Both results came from an analysis of data from the Solar Maximum Mission (SMM) Flat Crystal Spectrometer (FCS). However, analysis of FCS active region spectra by Schmelz et al. (1997) and by Saba et al. (1999) did not find the same disk-to-limb increase; moreover, with careful reexamination of several FCS spectra which the two studies have in common, and which sample a wide range of distances from disk center, we are unable to reproduce the results of Phillips et al. (1996, 1997) using standard FCS line fitting software; hence, we do not include their results in Table 14, believing they are in error. We note also that the theoretical intensities for the 15.02 Å line given in Table 1 of Phillips et al. (1997) are in error, although entries for the other lines are consistent with the calculations of Bhatia & Doschek (1992).

The prelaunch calibration of the FCS wavelength-dependent instrument sensitivity used in the analysis of Phillips et al. (1996, 1997) differs from the in-orbit updated calibration used by Schmelz et al. (1997) and Saba et al. (1999); this can account for a shift in the normalization of the Fe XVII line ratios (in the worst case, for 15.02/16.78, by over 30%) but it cannot explain a difference in the inferred center-to-limb behavior for data sets in common between the two studies. In any case, the difference in normalization of the 15.02/15.26 ratio resulting from the two different calibrations should be very small (less than 4%) owing to the small separation in wavelength of the two lines.

The pattern of behavior of the 15.02/15.26 ratio in Table 14 as a function of size of the FOV is not clear – in any case it is not monotonic. If the differences are not merely an artifact of different detector systematic uncertainties, variations in the way the observations were taken, or limited numbers of cases, then the behavior might reflect some geometrical effect determined by how the given FOV samples the source and scattering regions. The FCS 15-arcsec pixel corresponds to about 1.1×10^9 cm at the Sun, the size of a small coronal loop. The FCS spectral data included here were preferentially taken at the brightest pixel in the spatial raster done before the spectral scan. The modeling done by Wood & Raymond (2000) shows that, for optical depths of a few, this bright location could be either at the loop apex or over a loop footpoint of a medium-size loop, depending on the loop orientation with respect to the line of sight. The samples taken by Strong (1978) are for many locations in one or two active regions. The other pointings generally did not correspond to any preferred location within a region. In one case (Parkinson 1975), the pointing was offset two arcmin from the active region.

We note that most of the flare or post-flare ratios are systematically higher than most of the active region values; this is consistent with an increase in the ratio as a function of temperature, as predicted by the theoretical calculation for this temperature range (2-10 MK). The ratios for Capella (the brightest quiescent coronal X-ray source in the sky after the Sun) from Chandra observations – 2.64 ± 0.10 (Brinkman et al. 2000) and 2.72 ± 0.06 (Canizares et al. 2000) – are comparable to higher solar flare and post-flare values and the highest active region values, consistent with a derived temperature ($T_e \sim 6$ MK) intermediate between active region and flare temperatures.

We now use the FCS active region data set discussed by Schmelz et al. (1996) and Saba et al. (1999) as a convenient sample to compare with the updated theoretical calculations, and consider various ratios of the lines at 15.02, 15.26, 16.78, 17.05, and 17.10 Å. Figure 5 shows the FCS values for the 15.02/15.26 ratio with 1-σ errors plotted against the electron temperatures derived by Schmelz et al. (1996; see their Table 1) using Arnaud & Raymond (1992) ionization fractions; analysis discussed therein showed that these spectra could be treated as "effectively isothermal" in the regime of FCS sensitivity. Also included in the plot is the value determined by Waljeski et al. (1994) from other FCS data, shown by the diamond at T_e=2.5 MK. The measured values for the star Capella from Chandra observations (Brinkman et al. 2000, Canizares et al. 2000) are shown as asterisks at 6-6.3 MK; the 1-σ statistical errors on the ratio are smaller than the symbols. The theoretical curve for the ratio from the present calculation is shown as a solid curve; the dashed curve lies at 0.75 of the calculation, showing the approximate lower limit consistent with an estimated 25% uncertainty on the calculated ratio. The values for the ratio from the LLNL EBIT experiment (Brown et al. 1998) are plotted as bold crosses at the temperatures corresponding to the various beam energies (0.85-1.3 keV); the values from the NIST EBIT experiment (Laming et al. 2000) are plotted as triangles at the temperatures corresponding to the 0.9 keV and 1.25 keV beam energies. Although it is not rigorously correct to compare ratios obtained from theoretical calculations for a Maxwellian velocity distribution at a given temperature with ratios from measurements using nearly monoenergetic electron beams, we note that the EBIT measurements either touch the dashed curve or lie between the dashed and solid curves. The theoretical curves are more correctly compared with the solar and stellar line ratios, which are assumed to be produced in thermal plasmas. The Capella points are near the dashed curve, but the bulk of the FCS points lie below the dashed curve. The mean of the FCS observed values for the F(15.02)/F(15.26) ratio (ignoring variations in T_e) is 2.02 $\pm$ 0.03, where the quoted error is the error in the mean calculated for a normal distribution; the dispersion around the mean can be estimated from the standard deviation, = 0.28, and the goodness of fit to a constant value can be estimated from the reduced Chisquare (χ^2) for 32 degrees of freedom (see, e.g., Bevington 1969), = 1.64.

In Figure 6, the FCS 15.02/15.26 ratios which are summed in Table 14 have been individually divided by the present theory values for the measured temperatures, and then plotted as a function of θ across the disk, with 0° corresponding to disk center and 90° to the limb. Thus, a value of unity for this "theory normalized ratio" would mean that the measured ratio matches the present theoretical optically thin value. The near-limb value of Waljeski et al. (1994) from other FCS data is shown as a diamond. Because the theoretical ratio changes only gradually with temperature, increasing by less than 5% between 2 and 6 MK, the plot of the measured ratios as a function of θ looks very similar, with only minor details changed, except for the overall normalization.

The mean value of the observed 15.02/15.26 ratio relative to the new theoretical value is 0.54 $\pm$ 0.01, with a standard deviation of 0.07, and χ^2 = 1.57; the data/theory agreement is better by about 10% than before, comparing the same data to the earlier (1992) BD calculation, but the observed ratio is still about a factor of 2 too low. Note that Figure 2b of Saba et al. (1999) plots the inverted ratio 15.26/15.02 and the observed ratios there are not normalized by the temperature-dependent theory ratios (which are instead represented by horizontal lines indicating the calculated range expected for the relevant temperatures in the optically thin limit of the BD 1992 calculation). The two data points there with the largest uncertainties have been omitted here in Figure 6 to aid visual inspection of behavior as a function of θ. There appears to be a slight systematic trend of lower limb values than disk values, consistent with the trends shown in Table 14 (which includes the disk and limb averages of these FCS data).

4.2. *Other X-Ray Ratios*

In addition to 15.01/15.26, there are nine other distinct pairs of the five most prominent Fe XVII lines in the 15–17 Å band. In Figure 7, measured and calculated photon flux ratios for each of these nine pairs are plotted vs. T_e. Three additional ratios involving the sum of the 17.05 and 17.10 Å line intensities are included in the figure to allow a rough comparison with the NIST EBIT measurements in which the 17.05 Å and 17.10 Å lines were not resolved. For each ratio, for the sample of spectra considered above, the measured FCS values with 1-σ errors are shown as crosses; again the two most uncertain points are excluded from the plots to aid visual inspection.

although the values are included in the calculated means. The Capella ratio from Canizares et al. (2000) is shown as an asterisk (the 1-σ statistical error is smaller than the symbol); the NIST EBIT measurements are shown as triangles at temperatures corresponding to the 0.9 and 1.2 keV beam energies, for panels (a), (b), (j), (k), and (l). The solid curve gives the present optically thin theoretical calculation as a function of T_e, while the dashed curve is 0.75 or 1.33 times the theoretical curve, corresponding roughly to the expected theoretical uncertainty, for comparison with the measurements. In Figure 8, the observed FCS ratios for the same line pairs as in panels (a)-(i) of Figure 7 are divided by the respective current theory values for the temperatures measured by Schmelz et al. (1996) and plotted with 1-σ errors as functions of θ.

Referring to the panels in Figures 7 and 8, we detail some of the relevant quantities in Table 15 and discuss the various ratios briefly here:

- (a) F(15.02)/F(16.78): The FCS values lie below the solid theory curve, with an upper bound at about the dashed (0.75 $\times$ theory) curve, while the Capella value touches the dashed curve. The prediction has moved closer to the data, but the FCS observed ratio remains inconsistent with the optically thin prediction, by nearly a factor of 2.
- (b) F(15.26)/F(16.78): The FCS values bracket the solid curve while the Capella value lies on it. The observed FCS ratio was previously consistent with the optically thin prediction and remains so.
- (c) F(17.05)/F(16.78): The FCS values lie mostly above the solid theory curve and below the dashed (1.33 $\times$ theory) curve; the Capella value lies between the two curves. The current theory value is essentially unchanged from the previous value; the observed ratio remains within the uncertainty of the prediction.
- (d) F(15.02)/F(17.05): The FCS values and Capella value lie below the dashed (0.75 $\times$ theory) curve. The current theory value has moved closer to the observed ratio, but the data are still inconsistent with the optically thin calculation by about a factor of 2.
- (e) F(15.26)/F(17.05): The mean FCS value and the Capella value lie between the solid and dashed (0.75 $\times$ theory) curves, while the highest and lowest FCS points lie outside this band. The current theory value has moved closer to the observed ratio, and the two are now slightly more consistent.
- (f) F(17.10)/F(17.05): The mean FCS value and the Capella value lie above the solid theory curve, touching the dashed (1.33 $\times$ theory) curve; the solid theory curve gives a lower bound to the FCS values. [The mean observed FCS value for the inverse ratio – F(17.05)/F(17.10), not shown in Fig. 7 or 8 – is 1.05 $\pm$ 0.02, with a standard deviation of 0.12. This value is similar to values reported by Phillips et al (1982) for the 1980 Aug 25 flare (1.07) and an active region observed on 1980 Sep 23 (1.00).] The current theory value is nearly unchanged from the previous value; the observed ratio is marginally consistent with the prediction.
- (g) F(15.02)/F(17.10): The FCS values and the Capella value lie well below the dashed (0.75 $\times$ theory) curve. The current theory value has dropped by nearly 20%, moving closer to the observed ratio, but there is still a mismatch by about a factor of 3.
- (h) F(15.26)/F(17.10): The Capella value and most of the FCS values lie below the dashed (0.75 $\times$ theory) curve. The current theory value has moved closer to the observed ratio, but the latter still falls short, outside the expected uncertainty.
- (i) F(16.78)/F(17.10): The Capella value and most of the FCS values lie below the dashed (0.75 $\times$ theory) curve. The current theory value is essentially unchanged from the previous value, and the observed ratio falls short, outside the expected uncertainty.

For most of the ratios plotted in Figure 7, the Capella values lie at approximately the same distance from the theoretical curves as the mean of the FCS values (but at slightly higher T_e); the exceptions are those ratios involving the 15.02 Å line, where the Capella values are slightly closer to the curve than the FCS mean value. The ratios involving the 15.02 Å line also show the greatest variation about the mean, as shown by the larger values of χ^2, both for the photon ratios (Fig. 7) and the theory normalized ratios (Fig. 8).

5. DISCUSSION

5.1. *X-ray Data/Theory Comparison*

We can summarize the findings from the comparisons of the FCS data with the optically thin calculations in Section 4 as follows:

1. For those ratios involving only the 15.26, 16.78, and 17.05 Å lines (see panels b, c, and e in Figs. 7 and 8), the observed ratios seem largely consistent with the predicted ratios (within the uncertainties).

2. For those ratios involving the 15.02 Å line, all in the numerator (see Figs. 5 and 6 and panels a, d, and g in Figs. 7 and 8), the FCS mean values are well below the predicted ratios, suggesting that it is the observed 15.02 Å line which is lower than expected relative to the other lines, based on the optically thin calculations. There is also more scatter in these ratios, as evidenced by the larger values of χ^2. Some fraction of this is associated with slight systematic differences between disk and limb ratios.

3. For the ratios involving the 17.10 Å line in the denominator (see panels g, h, and i in Figs. 7 and 8), the mean observed ratios are substantially lower than the predictions (notably so for the 15.02/17.10 ratio shown in panel g); the mean observed 17.10/17.05 ratio shown in panel f of Figures 7 and 8, on the other hand, is marginally higher than predicted. Thus it appears that the 17.10 Å line intensity is observed to be higher than predicted, relative to the other lines.

One could argue that some of the individual discrepancies between the observed and calculated ratios could be attributed to potential problems with the FCS calibration, but that could not explain all of them, in particular not the ratio 15.02/15.26 where the wavelengths are close. Moreover, adjusting the calibration to improve the match for the observed 15.02/16.78 ratio would worsen it for the 15.26/16.78 ratio. The consistency of the observed ratios for 15.26/16.78 and 15.26/17.05 with the predicted values gives confidence that the calibration is not a serious issue. Thus it appears that there is a real discrepancy between the Fe XVII soft X-ray line observations and the optically thin calculations, particularly for ratios involving the 15.02 Å line, which is expected to be by far the most affected by opacity due to its large oscillator strength.

While again noting the caveat against comparing theoretical curves calculated for Maxwellian velocity distributions with monoenergetic beam measurements, we see that the EBIT ratios fall suggestively on or near the theoretical ratios, within the expected uncertainties, in Figure 5, and panels a, b, j, k, and l of Figure 7. For the line ratios considered in Figure 7 for which EBIT measurements are available, the stellar measurements of Capella by Canizares et al. (2000) seem typically somewhat more consistent with the FCS measurements than with the EBIT measurements where the three do not agree. (This echoes a finding by Laming et al. 2000 for a different combination of Fe XVII lines – see section 5.4) The EBIT measurements seem generally consistent with the optically thin theoretical curves even where the solar and stellar measurements do not.

A detailed comparison between the current theory and the EBIT measurements would require a recalculation at particular energies corresponding to beam energies, but such calculations would be less compatible with comparison with thermal emission lines from solar and stellar sources.

We have not so far considered comparisons between the observed and calculated ratios involving the fainter 15.45 Å line which was not readily measured in all of the FCS active region spectra in the sample examined. Here we note that the NIST EBIT measurements for ratios including this line disagree with the theoretical calculations by factors of 2-4, for both the calculations considered by Laming et al. (2000) and the present calculation. We note that this intersystem line, where both the angular momentum and the spin change, is harder to model than the resonance or forbidden lines.

5.2. *Solar Opacity Regime*

Because of the large oscillator strength of the 15.02 Å line (f=2.54), the high abundance of Fe [$A_{Fe_{ph}}$= N(Fe)/N(H) $\simeq 3.2\times10^{-5}$ in the photosphere (Anders & Grevesse 1989)], and the predominance of the Fe^{+16} ionization state over the range of active region temperatures, the optical depth of the 15.02 Å line is greater than unity for typical coronal conditions above solar active regions. This can be easily seen by rewriting Eq. (4) for τ, the optical depth at line center, in a form which can be readily evaluated for typical solar parameters:

$$\tau \approx 3.1 \times N_{10} L_{10} \left[\frac{I.F.}{0.69}\right] \left[\frac{A_{Fe}}{A_{Fe_{ph}}}\right] \sqrt{\frac{4}{T_6}}, \tag{9}$$

where $N_{10} = N_e/10^{10}$ cm^{-3}, $L_{10} = L/10^{10}$ cm, I.F. is the ionization fraction of N(Fe^{+16})/N(Fe) relative to its peak value of 0.69 at 4 MK (Arnaud & Raymond 1992), and T_6 is the Doppler temperature in MK.

In rewriting Eq.(4) as Eq. (9), we have used

$$N_1 = \left[\frac{N_1(^1S_0)}{N(Fe^{+16})}\right] \left[\frac{N(Fe^{+16})}{N(Fe)}\right] \left[\frac{N(Fe)}{N(H)}\right] \left[\frac{N(H)}{N_e}\right] N_e. \tag{10}$$

Since most of Fe XVII is in the lowest $2p^6\ ^1S_0$ level, we can take $N_1(^1S_0)/N(Fe^{+16}) \simeq 1$. Therefore,

$$N_1 = (I.F.)A_{Fe}(0.8)N_e \tag{11}$$

where we have taken N(H)/N$_e$=0.8 for a fully ionized plasma.

For $N_{10} = 1$, $L_{10} = 1$ (cf. the radius of the Sun, $L_{10} \approx 6.96$), and $T_6 = 4$, $\tau \sim 3$ for photospheric Fe abundance and scales directly with any Fe abundance enhancement in the corona; e.g., for Feldman (1992) coronal abundance, N(Fe)/N(H) = 10^{-4}, $\tau \sim 9.7$; for the Fludra & Schmelz (1999) "hybrid" abundance, N(Fe)/N(H) = 6.7×10^{-5}, $\tau \sim 6.4$. (For a higher Doppler temperature, τ and L_{10} would both be reduced by the factor $\sqrt{4/T_6}$.) In Fig. 4a, the peak of the 15.02/16.78 ratio for the cylindrical geometry occurs for $\tau \sim 5.2$, corresponding to $N_1 L \sim 3 \times 10^{15} cm^{-2}$ or $L_{10} \sim 0.6$ with N(Fe)/N(H) = 10^{-4} and all the other parameters as before. For $N_1 L \sim 3 \times 10^{16}$ ($L_{10} \sim 1.6$ with our given parameters) corresponding to $\tau \approx 50$, the optically thick curve for the cylindrical model has dropped back down to the optically thin value. The mean FCS observed ratio of 1.08 ($\sim$ 0.6 times the optically thin prediction) intersects the optically thick curve for the cylinder at $N_1 L \sim 3 \times 10^{17}$ or $L_{10} \sim 60$ and $\tau \sim 500$. This is an unrealistically large dimension ($\sim$ 8 solar radii) for the scattering volume, indicating that the theoretical calculation may still be somewhat too high (as suggested by the EBIT measurement, as noted above) or the isolated cylindrical model may be too simplified or both. Because the solar observations generally show reduced intensity in the 15.02 Å line compared to the theoretical value, if the discrepancy is due to a reduction in the line flux due to resonance scattering, then the typical coronal structure must preferentially scatter photons down to the solar surface. Wood & Raymond (2000) note that this would be consistent with emission from dense, low-lying loops that is scattered in a more diffuse, larger scale region, a situation that is observed in solar active regions. The relevance of such a scenario was also pointed out by Phillips et al. (1996).

5.3. *Complementary modeling of opacity*

Wood & Raymond (2000) modeled resonant scattering using a three-dimensional Monte Carlo radiation code for loop models developed by Rosner, Tucker, & Vaina (1978; hereinafter RTV); they find results which seem consistent with those presented here but which are carried further and which are easier to relate directly to observations: the optically thick intensity can vary by over a factor of two, ranging from 1.2 to 0.5 times the optically thin value, depending on T_{max} (the maximum temperature, which occurs at the loop apex in the RTV model) and the loop orientation; the results can be modified further by imbedding the loops in a background plasma, a more realistic scenario on the Sun than isolated loops. They note that, for an ensemble of loops with different orientations, the effects may tend to average out, especially since opacity can make loops look more uniform than in the optically thin case, but a net effect can persist when the emissivity and opacity, with their different dependences on electron density, don't vary in the same way. Nevertheless, the net effect may be small, which might explain why Fe XVII center-to-limb effects on the Sun are subtle. This might also suggest that dramatic effects from opacity are not expected for spatially integrated astrophysical observations.

5.4. *Other Recent Work*

Laming et al. (2000) extended another recent distorted wave 73-level model to a 113-level model and then to a 457-magnetic-sublevel model to take account of polarization. It should be noted that this 73-level model has collision strengths only at very high incident energies, above the threshold of the highest level (unpublished work of A. K. Bhatia 1999). Their theoretical results for the F(15.26)/F(15.02) ratio range from the case of zero polarization to maximum polarization. They indicate that the polarization corrections for the two lines in the recent NIST EBIT experiment are not significant and their measured ratio of 2.94 ± 0.18 at 0.9 keV is consistent with the average LLNL EBIT result of Brown et al. (1998).

In their Figure 3, Laming et al. (2000) compare distorted wave and R-matrix calculations with their NIST EBIT laboratory measurements of the ratio $(I_{16.78} + I_{17.05} + I_{17.10})/(I_{15.01} + I_{15.26} + I_{15.45})$ and they overplot observations of this ratio from the Sun and from Capella. The plot shows that (1) the stellar values are interspersed with the solar values, and (2) all the observed ratios but one lie systematically above, and most lie substantially above, the theoretical and laboratory ratios. The exception is the ratio taken from Phillips et al. (1982), for which those authors noted that the quoted line intensities were not yet calibrated and, furthermore, were obtained by scanning the lines during changing flare conditions. Thus there appears to be a general inconsistency between the reported solar and stellar values, and values obtained by laboratory measurements and (optically thin) theoretical modeling.

CONCLUSIONS

The atomic data obtained using 13 configurations which include n=2, 3, and 4 orbitals, have been used to compute the optically thick Fe XVII spectrum in a self-consistent manner using slab and cylindrical escape factors and escape probabilities. As indicated earlier by BK, the effects of opacity are somewhat less pronounced for cylindrical than for slab geometry because cylindrical escape probabilities are generally greater in magnitude than slab escape probabilties. The present calculations again indicate that the photon flux ratios F(15.02)/F(16.78) and F(15.26)/F(16.78) show an initial increase with increasing column length. The same predicted behavior is also seen for the lines at 12.262 and 12.122 Å. Predicted intensities for eleven lines in the extreme-ultraviolet 190–410 Å wavelength range, along with the forbidden line at 1154 Å, are found to be enhanced by opacity.

The LLNL and NIST EBIT laboratory measurements suggest that the present calculation of the F(15.02)/F(15.26) ratio in the optically thin limit is probably too high by about 25%; this is consistent with the expected uncertainty on a given calculated ratio. However, the 15.02/15.26 ratios from SMM FCS observations of solar active regions are still significantly below 0.75 of the optically thin prediction. For typical coronal conditions above active regions, the optical depth at line center of the 15.02 Å line should be substantially greater than unity, so opacity is a natural explanation for some of the discrepancies between the solar observations and the optically thin calculations. Detailed comparison of the optically thick calculations with the observations requires a more realistic treatment of the relevant geometry than is within the scope of this study, but the present analysis shows that the effects of moderate opacity can be both subtle and counter-intuitive at first glance.

It is important to understand that diagnostic ratios which are sensitive to opacity can have values which match the optically thin prediction even in the presence of moderate opacity, due to the competition between increased level population and decreased escape probability for the relevant lines. This can lead to misinterpretation of the physical conditions in the source environment unless independent checks are available.

Acknowledgements

This paper is a natural outgrowth of work begun with S. O. Kastner (deceased), our colleague and friend. This work was suported under NASA grant under Applied Information Systems Research Program under Contract W19,539.

References

Acton, L. W., Bruner, M. E., Brown, W. A., Fawcett, B. C., Schweizer, W., Speer, R. J. ApJ, **291**, 865.

Anders, E., & Grevesse, N. 1989, Geochim. Cosmochim. Acta, **53**, 197

Arnaud, M., & Raymond, J. 1992, ApJ, **398**, 394

Bevington, P. R. 1969, **Data Reduction and Error Analysis for the Physical Sciences**, McGraw-Hill

Bhatia, A. K., & Doschek, G. A. 1992, At. Data Nucl. Data Tables, **52**, 1

Bhatia, A. K., & Doschek, G. A. 2001, At. Data Nucl. Data Tables, (to be published)

Bhatia, A. K., & Kastner, S. O. 1997, J. Quant.Spectrosc.Rad.Tran., **58**, 347

Bhatia, A. K., & Kastner, S. O. 1999, ApJ, **516**, 482

Blake, R. L., Chubb, T. A., Friedman, H., & Unizicker, A. E. 1965, ApJ, **142**, 1

Brinkman, A. C et al. 2000, ApJ, **530**, L111

Brosius, J. W., Davila, J. M., Thomas, R. J., & Monsignori-Fossi, B. C. 1996, ApJS, **106**, 143

Brown, G. V., Beiersdorfer, P., Liedahl, D. A. & Widman, K. 1998, ApJ, **502**, 1015

Burgess, A., & Sheorey, B. V. 1974, J. Phys. B, **7**, 2403

Canizares, C. R., et al. 2000, ApJL, **539**, L41

Capriotti, E. R. 1965, ApJ, **142**, 1101

Doschek, G. A., Feldman, U., & Bhatia, A. K. 1991, Phys. Rev. A, 43, 2565

Doyle, J. G., & McWhirter, R. W. P. 1980, MNRAS, **193**, 947

Eissner, W., Jones, M., & Nussbaumer, H. 1972, Compt. Phys. Commun. **8**, 270

Eissner, W., & Seaton, M. J. 1979, J. Phys. B, **5**, 2187

Eissner, W. 1998, Comput. Phys. Commun., **114**, 295

Feldman, U. 1992, Phys. Scr. **46**, 202

Feldman, U., Doschek, G. A., & Seely, J. F. 1985, MNRAS, 212, 41P

Fludra, A. & Schmelz, J. T. 1999, A&A, **348**, 286

Hagelstein, P. L., & Jung, R. K. 1987, At. Data Nucl. Data, Tables, **37**, 121

Hutcheon, R. H., Pye, F. P., & Evans, K. D. 1976, MNRAS, **175**, 489

Jupen, C., & Litzen, U. 1984, Phys. Scr. **30**, 112

Kaastra, J.S., Mewe, R., Liedahl, D. A., Komossa, S. & Brinkman, A. C. 2000, A&A, **354**, L83

Kahn, S. M., Leutenegger, M. A., Cottom,, J., Rauw, G., Vreux, J. -M., den Boggende, A. J. F., Mewe, R., & Güdel, M. 2000, A &A, (to appear)

Kaspi, S., Brandt, W. N., Netzer, H., Sambruna, R., Chartas, G., Garmire, G., & Nousek, J. 2000, ApJ, **535**, L17

Kastner, S. O., & Kastner, R. E. 1990, J. Quant.Spectrosc.Rad.Tran., **44**, 275

Laming, J. M., et al. 2000, ApJL, **545**, L161

Liedahl, D. A. 2000, Proc. At. Data Needs for X-ray Astronomy, Ed. Bautista, M. A., Kallman, T. R., & Pradhan, A. K., p. 151

McKenzie, D. L, Landecker, P. B., Broussard, R. M., Rugge, H. R., & Young, R. M. 1980, ApJ, **241**, 409

Parkinson, J. H. 1975, Sol. Phys., **42**, 183

Phillips, K. J. H., Leibacher, J. W., Wolfson, C. J., Parkinson, J. H., Fawcett, B. C., Kent, B. J., Mason, H. E., Acton, L. W., Culhane, J.L., & Gabriel, A. H. 1982, ApJ, **256**, 774

Phillips, K. J. H., Greer, C. J., Bhatia, A. K., & Keenan, F. P. 1996, ApJL, **469**, L57

Phillips, K. J. H., Greer, C. J., Bhatia, A. K., Coffey, I. H., Barnsley, R., & Keenan, F. P. 1997, A&A, **324**, 381

Rosner, R., Tucker, W. H. and Vaiana, G. S. 1978, ApJ, 220, 643

Rugge, H. R., & McKenzie, D. L. 1985, ApJ, **297**, 338

Saba, J. L. R., Schmelz, J. T., Bhatia, A. K., & Strong, K. T. 1999, ApJ, **510**, 1064

Saraph, H. E. 1978, Comput. Phys. Commun., **15**, 247

Saraph, H. E., & Eissner, W. 2001 Comput. Phys. Commun. (to be published)

Schmelz, J. T., Saba, J. L. R., Ghosh, D., & Strong, K. T. 1996, ApJ, **473**, 519

Strong, K. T. 1978, Ph. D. thesis, Univ. College London

Sugar, J., & Corliss, C. 1985, J. Phys. Chem. Ref. Data **14**, Suppl. No. 2

Thomas, R. J., & Neupert, W. M. 1994, ApJS, **91**, 461

Waljeski, K., Moses, D., Dere, K. P., Saba, J. L. R., Webb, D. F., Zarro, D. M. 1994, ApJ, **429**, 909.

Walker, A. B. C., Rugge, H. R., & Weiss, K. 1974, Ap. J., **194**, 471.

Wood, K., & Raymond, J. 2000 ApJ **540**, 563

Zhang, H., Sampson,D. H., Clark, R. E. H.& Mann, J. B. 1987, At. Data Nucl. Data, Tables, **37**, 17

Zhang, H. & Sampson, D. H. 1989, At. Data Nucl. Data, Tables, **43**, 1

Table 1

CALCULATED AND OBSERVED ENERGY LEVELS

Key	Configuration	Level	Energy (cm^{-1}) E(37)[a]	E(73)[b]	E(obs)[c]
1	$2p^6$	$^1S_0$	0.	0.	0.
2	$2p^53s$	$^3P_2$	5855681.	5852294.	5849320.
3	$2p^53s$	$^1P_1$	5871662.	5868335.	5864590.
4	$2p^53s$	$^3P_0$	5956518.	5952927.	5951310.
5	$2p^53s$	$^3P_1$	5967008.	5963262.	5960870.
6	$2p^53p$	$^3S_1$	6099089.	6095168.	6093410.
7	$2p^53p$	$^3D_2$	6128677.	6125451.	6121610.
8	$2p^53p$	$^3D_3$	6141047.	6137775.	6134630.
9	$2p^53p$	$^3P_1$	6150493.	6147585.	6143730.
10	$2p^53p$	$^3P_2$	6164853.	6161825.	6158360.
11	$2p^53p$	$^3P_0$	6211008.	6207484.	6202450.
12	$2p^53p$	$^1P_1$	6225625.	6222016.	6219110.
13	$2p^53p$	$^3D_1$	6250816.	6247355.	6245320.
14	$2p^53p$	$^1D_2$	6254324.	6250675.	6248350.
15	$2p^53p$	$^1S_0$	6382883.	6374405.	6353230.
16	$2p^53d$	$^3P_0$	6471451.	6468769.	6463490.
17	$2p^53d$	$^3P_1$	6479930.	6476686.	6472100.
18	$2p^53d$	$^3P_2$	6495791.	6491970.	6486290.
19	$2p^53d$	$^3F_4$	6497860.	6493999.	6486530.
20	$2p^53d$	$^3F_3$	6502404.	6499488.	6492790.
21	$2p^53d$	$^3D_2$	6516087.	6513514.	6506650.
22	$2p^53d$	$^3D_3$	6526494.	6523000.	6515320.
23	$2p^53d$	$^3D_1$	6564054.	6560333.	6555200.
24	$2p^53d$	$^3F_2$	6602675.	6599593.	6594460.
25	$2p^53d$	$^1D_2$	6610544.	6606553.	6602000.
26	$2p^53d$	$^1F_3$	6615598.	6611578.	6606500.
27	$2p^53d$	$^1P_1$	6679234.	6673755.	6661300.
28	$2s2p^63s$	$^3S_1$	6951738.	6948985.	6948900.
29	$2s2p^63s$	$^1S_0$	7005493.	7001777.	7001700.
30	$2s2p^63p$	$^3P_0$	7216068.	7213999.	7213500.
31	$2s2p^63p$	$^3P_1$	7219978.	7217680.	7199400.
32	$2s2p^63p$	$^3P_2$	7238595.	7236016.	7236100.
33	$2s2p^63p$	$^1P_1$	7254052.	7251901.	7233800.
34	$2s2p^63d$	$^3D_1$	7580521.	7578907.	
35	$2s2p^63d$	$^3D_1$	7582528.	7580269.	
36	$2s2p^63d$	$^3D_1$	7585978.	7582871.	
37	$2s2p^63d$	$^3D_1$	7625118.	7622552.	

[a]Energy levels obtained using seven configurations.

[b]Energy levels obtained using thirteen configurations.

[c]Observed energy levels obtained by Jupen & Litzen 1984.

Table 2
CALCULATED ENERGY LEVELS

Key	Configuration	Level	E(73)[a]	Energy (cm^{-1}) E(obs)
38	$2s^22p^54s$	$^3P_2$	7884533.	
39	$2s^22p^54s$	$^1P_1$	7889764.	7885800.[b]
40	$2s^22p^54s$	$^3P_0$	7985195.	
41	$2s^22p^54p$	$^3S_1$	7986323.	
42	$2s^22p^54s$	$^3P_1$	7987890.	7985945.[c]
43	$2s^22p^54p$	$^1D_2$	7993429.	
44	$2s^22p^54p$	$^3D_3$	7998481.	
45	$2s^22p^54p$	$^1P_1$	8001858.	
46	$2s^22p^54p$	$^3P_2$	8006519.	
47	$2s^22p^54p$	$^3P_1$	8039148.	
48	$2s^22p^54p$	$^3D_1$	8092097.	
49	$2s^22p^54p$	$^3P_1$	8101156.	
50	$2s^22p^54p$	$^3D_2$	8103016.	
51	$2s^22p^54d$	$^3P_0$	8121739.	
52	$2s^22p^54d$	$^3P_1$	8125204.	8116000.[b]
53	$2s^22p^54d$	$^3F_4$	8129763.	
54	$2s^22p^54p$	$^1S_0$	8130236.	
55	$2s^22p^54d$	$^3P_2$	8130969.	
56	$2s^22p^54d$	$^1F_3$	8131825.	
57	$2s^22p^54d$	$^3D_2$	8136791.	
58	$2s^22p^54d$	$^3D_3$	8140001.	
59	$2s^22p^54d$	$^3D_1$	8161248.	8154611.[c]
60	$2s^22p^54d$	$^3F_2$	8231402.	
61	$2s^22p^54d$	$^1D_2$	8233573.	
62	$2s^22p^54d$	$^3F_3$	8236097.	
63	$2s^22p^54d$	$^1P_1$	8254364.	8249463.[c]
64	$2s2p^64s$	$^3S_1$	8965868.	
65	$2s2p^64s$	$^1S_0$	8984318.	
66	$2s2p^64p$	$^3P_0$	9073052.	
67	$2s2p^64p$	$^3P_1$	9074302.	9056000.[b]
68	$2s2p^64p$	$^3P_2$	9081655.	
69	$2s2p^64p$	$^3S_1$	9086920.	9072000.[b]
70	$2s2p^64d$	$^3S_1$	9209427.	
71	$2s2p^64d$	$^3D_2$	9210009.	
72	$2s2p^64d$	$^3D_3$	9211124.	
73	$2s2p^64d$	$^1D_2$	9225131.	

[a] Energy levels obtained using thirteen configurations.
[b] NIST compilation (Sugar & Corliss 1985).
[c] Observed energy levels obtained by Phillips et al. 1982.

Table 3

OSCILLATOR STRENGTHS AND RADIATIVE TRANSITION RATES OBTAINED USING 7 AND 13 CONFIGURATIONS

Transition($j \rightarrow i$)	$\lambda(\AA)$	f(i,j)[a]	A(j,i)[a]	f(i,j)[b]	A(j,i)[b]
2→1	17.10	4.000-8	1.690+05	4.000-8	1.690+05
3→1	17.05	1.230-1	9.441+11	1.236-1	9.463+11
5→1	16.78	1.010-1	8.008+11	1.033-1	8.168+11
7→1	16.34		5.277+08		5.094+08
17→1	15.45	8.859-3	8.270+10	9.568-3	8.923+10
23→1	15.26	5.930-1	5.685+12	6.025-1	5.765+12
27→1	15.02	2.662+0	2.641+13	2.541+0	2.516+13

[a]Oscillator strengths and radiative rates obtained using seven configurations.
[b]Oscillator strengths and radiative rates obtained using thirteen configurations.

Table 4

COLLISION STRENGTHS AT VARIOUS INCIDENT ELECTRON ENERGIES[a]

Transition(j → i)	Collision Strength					
1 → 2	1.873-3	1.599-3	1.549-3	1.418-3	1.249-3	7.528-4
	5.036-4	3.591-4	2.684-4	1.657-4	1.122-4	
1 → 3	1.967-3	2.192-3	2.383-3	2.637-3	3.030-3	4.873-3
	6.531-3	7.978-3	9.246-3	1.138-2	1.313-2	
1 → 5	1.859-3	2.084-3	2.244-3	2.433-3	2.737-3	4.204-3
	5.548-3	6.732-3	7.777-3	9.546-3	1.099-2	
1 → 7	4.200-3	3.732-3	3.726-3	3.599-3	3.456-3	3.199-3
	3.204-3	3.275-3	3.359-3	3.514-3	3.637-3	
1 →17	0.000+0	6.479-3	5.680-3	5.111-3	4.466-3	2.747-3
	2.046-3	1.726-3	1.577-3	1.534-3	1.699-3	
1 →23	0.000+0	2.200-2	2.326-2	2.488-2	2.744-2	3.754-2
	4.577-2	5.266-2	5.856-2	6.826-2	7.596-2	
1 →27	0.000+0	8.463-2	9.077-2	9.787-2	1.086-1	1.522-1
	1.870-1	2.160-1	2.408-1	2.818-1	3.147-1	

[a]Incident electron energies are 58.5, 65.0, 70.0, 76.0, 85.0, 127.5, 17.0, 212.5, 255.0, 340.0, and 425.0 Ry.

Table 5
INTENSITY RATIOS FOR X-RAY LINES[a]

Transition($j \to i$)	λ(Å)	Intensity Ratio				
		27[b]	37[b]	63[b]	73[b]	37[c]
$2 \to 1$	17.10	8.085-1	8.057-1	8.010-1	8.098-1	7.960-1
$3 \to 1$	17.05	1.128+0	1.190+0	1.162+0	1.165+0	1.192+0
$5 \to 1$	16.78	1.000+0	1.000+0	1.000+0	1.000+0	1.000+0
$7 \to 1$	16.34	2.124-2	2.268-2	2.177-2	2.196-2	2.320-2
$17 \to 1$	15.45	1.110-1	9.586-2	8.716-2	8.673-2	9.290-2
$23 \to 1$	15.26	6.653-1	5.573-1	5.097-1	5.068-1	5.560-1
$27 \to 1$	15.02	2.554+0	2.114+0	1.904+0	1.893+0	2.260+0

[a]Intensity ratios (in photon units) are normalized to the intensity of the allowed line at 16.78 Å.
[b]Entries 27, 37, 63, and 73 refer to the number of levels used in the present calculation of intensity ratios.
[c]Intensity ratios for 37 levels from Bhatia & Doschek 1992 calculation.

Table 6

VARIATION OF INTENSITY RATIOS[a] FOR X-RAY LINES WITH ELECTRON DENSITY[b]

Transition($j \rightarrow i$)	λ(Å)	Intensity Ratio					
		8	9	10	11	12	13
$2 \rightarrow 1$	17.10	8.11-1	8.11-1	8.11-1	8.10-1	7.97-1	7.09-1
$3 \rightarrow 1$	17.05	1.17+0	1.17+0	1.17+0	1.17+0	1.13+0	1.09+0
$5 \rightarrow 1$	16.78	1.00+0	1.00+0	1.00+0	1.00+0	1.00+0	1.00+0
$7 \rightarrow 1$	16.34	2.20-2	2.20-2	2.20-2	2.20-2	2.21-2	2.56-2
$17 \rightarrow 1$	15.45	8.69-2	8.69-2	8.69-2	8.67-2	8.55-2	8.42-2
$23 \rightarrow 1$	15.26	5.08-1	5.08-1	5.08-1	5.07-1	4.98-1	4.79-1
$27 \rightarrow 1$	15.02	1.90+0	1.90+0	1.90+0	1.89+0	1.86+0	1.79+0

[a]Intensity ratios (in photon units) are normalized to the intensity of the allowed line at 16.78 Å.

[b]Column headings are $\log N_e (cm^{-3})$.

Table 7
VARIATION OF INTENSITY RATIOS FOR X-RAY LINES[a] WITH ELECTRON TEMPERATURE[b]

Transition($j \rightarrow i$)	λ(Å)	Intensity Ratio				
		2×10^6	3×10^6	4×10^6	5×10^6	6×10^6
$2 \rightarrow 1$	17.10	8.78-1	8.40-1	8.10-1	7.82-1	7.57-1
$3 \rightarrow 1$	17.05	1.19+0	1.17+0	1.17+0	1.16+0	1.15+0
$5 \rightarrow 1$	16.78	1.00+0	1.00+0	1.00+0	1.00+0	1.00+0
$7 \rightarrow 1$	16.34	2.26-2	2.22-2	2.20-2	2.17-2	2.14-2
$17 \rightarrow 1$	15.45	9.83-2	9.21-2	8.67-2	8.21-2	7.80-2
$23 \rightarrow 1$	15.26	4.64-1	4.87-1	5.07-1	5.25-1	5.43-1
$27 \rightarrow 1$	15.02	1.66+0	1.79+0	1.89+0	1.98+0	2.07+0

[a]Intensity ratios (in photon units) are normalized to the intensity of the allowed line at 16.78 Å.
[b]Column headings are electron temperatures in K.

Table 8A

VARIATION OF INTENSITY RATIOS OF X-RAY LINES[a] WITH ELECTRON DENSITY

Transition[b]	λ(Å)	10^8	10^9	10^{10}	10^{11}	10^{12}	10^{13}
2→1	17.096	9.610-1	9.609-1	9.606-1	9.574-1	9.320-1	8.008-1
3→1	17.051	1.225+0	1.224+0	1.224+0	1.215+0	1.164+0	1.137+0
5→1	16.788	1.000+1	1.000+0	1.000+0	1.000+0	1.000+0	1.000+0
7→1	16.336	2.331-2	2.331-2	2.331-2	2.331-2	2.358-2	2.947-2
10→1	16.238	1.492-2	1.492-2	1.492-2	1.493-2	1.526-2	2.024-2
14→1	16.004	1.853-2	1.853-2	1.853-2	1.847-2	1.808-2	1.740-2
17→1	15.450	1.028-1	1.028-1	1.027-1	1.024-1	1.002-1	9.778-2
18→1	15.417	7.622-3	7.622-3	7.619-3	7.595-3	7.438-3	7.256-3
23→1	15.255	4.142-1	4.142-1	4.141-1	4.126-1	4.029-1	3.846-1
27→1	15.012	1.378+0	1.378+0	1.377+0	1.372+0	1.340+0	1.278+0
31→1	13.890	6.419-3	6.419-3	6.417-3	6.394-3	6.245-3	5.969-3
33→1	13.824[c]	2.041-2	2.041-2	2.040-2	2.033-2	1.985-2	1.894-2
37→1	13.119[c]	3.594-3	3.594-3	3.593-3	3.580-3	3.496-3	3.335-3
39→1	12.675[c]	7.356-4	7.356-4	7.353-4	7.328-4	7.159-4	6.866-4
42→1	12.522[d]	4.639-4	4.639-4	4.638-4	4.622-4	4.519-4	4.323-4
52→1	12.307[c]	2.478-4	2.478-4	2.477-4	2.468-4	2.414-4	2.337-4
59→1	12.263[d]	2.285-2	2.284-2	2.284-2	2.275-2	2.222-2	2.120-2
63→1	12.122[d]	2.473-2	2.473-2	2.472-2	2.463-2	2.405-2	2.295-2
69→1	11.005[c]	3.255-4	3.255-4	3.254-4	3.242-4	3.166-4	3.020-4

[a] Intensities relative to line at 16.78 Å are in photon units at $T_e = 10^6$ K; column headings are electron densities in cm^{-3}.

[b] Keyed to Tables 1 and 2.

[c] Calculated wavelengths, NIST values are 12.681, 12.321, 11.042, 11.023 Å.

[d] Observed wavelengths from Phillips et al. 1982.

Table 8B

VARIATION OF INTENSITY RATIOS OF X-RAY LINES[a] WITH ELECTRON DENSITY

Transition[b]	λ(Å)	10^8	10^9	10^{10}	10^{11}	10^{12}	10^{13}
2→1	17.096	6.737-1	6.737-1	6.736-1	6.733-1	6.689-1	6.158-1
3→1	17.051	1.142+0	1.142+0	1.141+0	1.138+0	1.113+0	1.084+0
5→1	16.788	1.000+1	1.000+0	1.000+0	1.000+0	1.000+0	1.000+0
7→1	16.336	2.059-2	2.059-2	2.059-2	2.059-2	2.068-2	2.280-2
10→1	16.238	1.442-2	1.442-2	1.443-2	1.444-2	1.463-2	1.725-2
14→1	16.004	1.998-2	1.998-2	1.998-2	1.996-2	1.979-2	1.942-2
17→1	15.450	6.574-2	6.574-2	6.573-2	6.566-2	6.541-2	6.466-2
18→1	15.417	4.943-3	4.942-3	4.942-3	4.937-3	4.900-3	4.866-3
23→1	15.255	6.092-1	6.092-1	6.091-1	6.083-1	6.022-1	5.861-1
27→1	15.012	2.362+0	2.362+0	2.362+0	2.358+0	2.335+0	2.272+0
31→1	13.890	2.438-2	2.438-2	2.438-2	2.435-2	2.410-2	2.347-2
33→1	13.824	1.750-1	1.750-1	1.749-1	1.747-1	1.729-1	1.683-1
37→1	13.119[c]	1.962-2	1.962-2	1.962-2	1.959-2	1.939-2	1.887-2
39→1	12.675[c]	8.421-3	8.421-3	8.420-3	8.409-3	8.325-3	8.109-3
42→1	12.522[d]	4.374-3	4.374-3	4.373-3	4.368-3	4.325-3	4.213-3
52→1	12.307[c]	1.327-3	1.327-3	1.327-3	1.326-3	1.315-3	1.302-3
59→1	12.263[d]	2.477-1	2.477-1	2.476-1	2.473-1	2.448-1	2.382-1
63→1	12.122[d]	3.011-1	3.011-1	3.011-1	3.007-1	2.977-1	2.897-1
67→1	11.020[c]	2.009-3	2.009-3	2.009-3	2.006-3	1.986-3	1.932-3
69→1	11.005[c]	1.815-2	1.815-2	1.815-2	1.812-2	1.794-2	1.746-2
73→1	10.840[c]	2.400-4	2.400-4	2.400-4	2.396-4	2.372-4	2.308-4

[a] Intensities relative to line at 16.78 Å are in photon units at $T_e = 10^7$ K; column headings are electron densities in cm^{-3}.

[b] Keyed to Table 1 and 2.

[c] Calculated wavelengths, NIST values are 12.681, 12.321, 11.042, 11.023 Å.

[d] Observed wavelengths from Phillips et al. 1982.

Table 9
EUV LINES AND RELATIVE INTENSITIES[a]

Transition[b] (j → i)	λ(Å)	Intensity Ratio[c]	Intensity Ratio[d]
27 → 9	193.7		1.911-4
15 → 3	204.65	6.051-1	4.201-1
27 → 12	226.1		4.444-4
27 → 13	240.4		2.412-4
23 → 9	243.0		6.567-4
18 → 6	254.5	8.970-2	6.013-2
15 → 5	254.87	6.552-1	4.615-1
21 → 7	260.	3.715-2	2.647-2
24 → 12	266.42	7.816-2	5.593-2
20 → 7	269.41	1.414-1	1.012-1
16 → 6	269.88	4.236-2	3.045-2
21 → 9	275.54	6.281-2	4.291-2
26 → 14	279.2	1.499-1	1.071-1
22 → 10	279.4	1.163-1	8.261-2
25 → 13	280.4	8.690-2	6.205-2
19 → 8	284.17	1.731-1	1.235-1
11 → 3	295.98	7.925-2	6.464-2
18 → 10	305.0	5.730-2	3.956-2
10 → 2	323.57	1.519-1	1.171-1
27 → 15	324.5		2.589-4
13 → 4	340.1	8.017-2	6.516-2
10 → 3	340.4	1.101-1	8.566-2
14 → 5	347.85	2.497-1	1.938-1
8 → 2	350.5	3.747-1	2.938-1
13 → 5	351.6	4.603-2	3.717-2
9 → 3	358.24	1.147-1	9.581-2
7 → 2	367.26	1.147-1	1.122-1
12 → 4	373.41	5.585-2	4.450-2
12 → 5	387.23	7.244-2	5.882-2
7 → 3	389.08	1.388-1	1.071-1
6 → 2	409.69	2.488-1	1.984-1

[a] Intensities in photon units at $T_e = 4 \times 10^6 K$, $N_e = 10^{11} cm^{-3}$

[b] Keyed to Table 1.

[c] Entries are log[F(λ)/F(17.10)] from Bhatia and Kastner 1999.

[d] Entries are log[F(λ)/F(17.10)] from 13-configuration calculation.

Table 10

X-RAY PHOTON FLUX RATIOS[a] IN SLAB GEOMETRY[b]

log (N_1L)[c]	17.05	16.78	15.45	15.26	15.02	13.82
$-\infty$	0.158	0.0916	-0.970	-0.204	0.369	-0.914
13	0.159	0.0925	-0.970	-0.200	0.380	-0.912
14	0.165	0.0977	-0.970	-0.182	0.428	-0.903
15	0.200	0.127	-0.966	-0.103	0.566	-0.858
16	0.329	0.242	-0.947	0.0336	0.627	-0.747
17	0.484	0.384	-0.888	0.0182	0.598	-0.877
18	0.607	0.469	-0.999	-0.199	0.370	-1.488
19	0.703	0.538	-1.622	-0.856	-0.267	-2.406
20	0.714	0.544	-2.492	-1.752	-1.167	-3.350
21	0.720	0.549	-3.437	-2.704	-2.123	-4.305

[a] Entries are log [F(λ)/F(17.10)]; column headings are line wavelengths (Å).

[b] $T_e = 4 \times 10^6 K$, $N_e = 10^{11} cm^{-3}$.

[c] N_1L is the column density (cm^{-2}) of Fe XVII.

Table 11

X-RAY PHOTON FLUX RATIOS[a] IN CYLINDRICAL GEOMETRY[b]

log (N_1L)[c]	17.05	16.78	15.45	15.26	15.02	13.82
-∞	0.158	0.0916	-0.9700	-0.204	0.369	-0.914
13	0.158	0.0918	-0.970	-0.203	0.371	-0.914
14	0.159	0.0928	-0.970	-0.198	0.389	-0.912
15	0.171	0.103	-0.970	-0.163	0.465	-0.896
16	0.244	0.163	-0.967	-0.082	0.515	-0.847
17	0.379	0.276	-0.958	-0.102	0.466	-1.000
18	0.510	0.368	-1.116	-0.389	0.171	-1.704
19	0.578	0.412	-1.803	-1.152	-0.598	-2.696
20	0.579	0.410	-2.763	-2.126	-1.573	-3.706
21	0.568	0.398	-3.767	-3.132	-2.579	-4.715

[a] Entries are log [F(λ)/F(17.10)]; column headings are line wavelengths (Å).

[b] $T_e = 4 \times 10^6 K, N_e = 10^{11} cm^{-3}$.

[c] N_1L is the column density (cm^{-2}) of Fe XVII.

Table 12
EUV PHOTON FLUX RATIOS[a] IN CYLINDRICAL GEOMETRY[b]

Transition	(λ(Å)	log(Fe XVII column density(cm^{-2}))							
j→i		-∞	16	17	18	19	20	21	22
4→3	1154.	-0.605	-0.580	-0.458	-0.200	-0.071	-0.051	-0.049	-0.049
9→3	358.2	-0.683	-0.636	-0.464	-0.201	-0.077	-0.058	-0.056	-0.055
11→3	296.0	-0.854	-0.785	-0.589	-0.381	-0.284	-0.269	-0.268	-0.267
12→4	373.41	-1.016	-0.975	-0.795	-0.467	-0.317	-0.295	-0.293	-0.292
13→4	340.1	-0.850	-0.830	-0.730	-0.508	-0.392	-0.374	-0.372	-0.372
12→5	387.2	-0.895	-0.854	-0.674	-0.345	-0.196	-0.174	-0.171	-0.171
13→5	351.6	-1.094	-1.074	-0.974	-0.752	-0.636	-0.618	-0.616	-0.616
23→9	243.0	-2.847	-2.200	-1.370	-0.702	-0.483	-0.452	-0.449	-0.449
27→9	193.7	-3.474	-2.291	-1.392	-0.721	-0.506	-0.477	-0.474	-0.474
27→13	240.4	-3.282	-2.098	-1.199	-0.528	-0.313	-0.284	-0.281	-0.281
27→15	324.5	-3.251	-2.067	-1.168	-0.497	-0.283	-0.253	-0.250	-0.250
27→12	226.1	-3.016	-1.833	-0.934	-0.263	-0.048	-0.019	-0.016	-0.015

[a] Entries are log [F(λ)/F(254.9)].
[b] $T_e = 4 \times 10^6 K, N_e = 10^{11} cm^{-3}$.

Table 13

PHOTON FLUX[a] OF EUV LINES UNAFFECTED BY OPACITY

Transition[b]	$\lambda(\AA)$	Optically Thin[c]	multicolumn1Factor[d]
15→3	204.65	0.519	1.213
18→6	254.5	0.074	0.824
15→5	254.87	0.570	1.213
21→7	260.	0.033	0.828
24→12	266.42	0.069	0.834
20→7	269.41	0.125	0.824
16→6	269.88	0.038	0.824
21→9	275.54	0.053	0.828
26→14	279.2	0.132	0.826
22→10	279.4	0.102	0.824
25→13	280.4	0.077	0.832
19→8	284.17	0.152	0.824
18→10	305.	0.049	0.824
10→2	323.57	0.145	0.955
10→3	340.40	0.106	0.957
14→5	347.85	0.239	0.991
8→2	350.5	0.363	0.824
7→2	367.2	0.139	0.979
7→3	389.08	0.132	0.979
6→2	409.69	0.245	1.059

[a] $T_e = 4 \times 10^6 K, N_e = 10^{11} cm^{-3}$.

[b] Keyed to Table 1.

[c] Entries are $F(\lambda)/F(17.10)$ in photon units.

[d] Change in photon flux from optically thin value for $N_1L=10^{18}$ cm^{-2} (greater than solar radius).

Table 14: Measured Fe XVII 15.02/15.26 Å Photon Intensity Ratios

Solar Active Regions

Disk Values	No. Samples	Limb Values[a]	No. Samples	FOV	Reference
2.14 ± 0.22^b	25[c]	1.80 ± 0.18^b	6	15"	1
1.87 ± 0.21	1	—	–	15"	2
2.56 ± 0.28^b	7	2.29 ± 0.21^b	5	35"	3
2.13	35[d]	—	–	60"	4
1.95 ± 0.06^b	8	1.80 ± 0.06^b	6	148"	3
2.13 ± 0.10	1[e]	—	–	180"	5
2.40 ± 0.10	2[d]	—	–	180"	6
1.61 ± 0.32	1	—	–	>30'	7
2.36, 1.78	2	—	–		8

Solar Flaring/Post-flare Active Regions

Disk Values	No. Samples	Limb Values[a]	No. Samples	FOV	Reference
1.73	1	—	–	1.2"×28"	9
2.75 ± 0.13	11	—	–	40"	3
2.75 ± 0.68	1	—	–	60"	10
2.67 ± 0.05	1[d]	—	–	180"	6

REFERENCES

(1) Saba et al. 1999 (SMM Flat Crystal Spectrometer).
(2) Waljeski et al. 1994 (SMM Flat Crystal Spectrometer).
(3) Strong 1978 (Aerobee rocket).
(4) Rugge & McKenzie 1985 (P78-1 SOLEX).
(5) Parkinson 1975 (Sounding rocket).
(6) Hutcheon, Pye, & Evans 1976 (Skylark rocket).
(7) Blake et al. 1965 (Aerobee rocket).
(8) Walker, Rugge, & Weiss 1974 (OVI-10, OVI-17 satellites)
(9) Acton et al. 1985 (Sounding rocket)
(10) McKenzie et al. 1980 (P78-1 SOLEX).

FOOTNOTES

(a) Limb regions have $\theta \geq 85$ °.
(b) Quoted error is the square root of the variance/N.
(c) Two disk measurements with large uncertainties omitted.
(d) No information on region location.
(e) FOV offset 2' from active region.

TABLE 15
OBSERVED AND CALCULATED Fe XVII PHOTON FLUX RATIOS.

Observed photon flux ratio					
Lines (Å)	Weighted mean	Error in mean	Standard deviation	Reduced χ^2	T_e factor[a]
15.02/16.78	1.04	0.02	0.13	2.38	1.19
15.26/16.78	0.51	0.01	0.08	0.93	1.13
17.05/16.78	1.40	0.02	0.20	0.76	0.97
15.02/17.05	0.74	0.01	0.11	2.59	1.22
15.26/17.05	0.36	0.01	0.06	1.30	1.16
17.10/17.05	0.93	0.02	0.11	0.95	1.09
15.02/17.10	0.78	0.01	0.11	2.73	1.34
15.26/17.10	0.38	0.01	0.06	1.18	1.27
16.78/17.10	0.75	0.01	0.07	0.55	1.12

Observed ratio/calculated ratio					
Lines (Å)	Weighted mean	Error in mean	Standard deviation	Reduced χ^2	New/old factor[b]
15.02/16.78	0.56	0.01	0.07	2.10	0.84
15.26/16.78	1.01	0.02	0.16	1.03	0.91
17.05/16.78	1.19	0.02	0.17	0.75	0.98
15.02/17.05	0.46	0.01	0.07	2.38	0.86
15.26/17.05	0.84	0.02	0.14	1.44	0.93
17.10/17.05	1.33	0.02	0.16	1.02	1.04
15.02/17.10	0.34	0.01	0.05	2.54	0.82
15.26/17.10	0.62	0.01	0.11	1.52	0.90
16.78/17.10	0.61	0.01	0.06	0.63	1.01

[a] Factor increase in predicted ratio as T_e increases from 2 to 5 MK, the range of temperatures for the active regions in the FCS sample.

[b] New optically thin theoretical ratio from present 73-level calculation, compared with previous ratio from 37-level BD calculation.

Figure Captions

Fig. 1. Collision strengths (Ω) for the transition $2p^6(^1S_0) \rightarrow 2p^5 3s(^3P_1)$. The solid line represents the present calculation with 13 configurations and the * represent Ω obtained using 7 configurations (Bhatia & Doschek 1992).

Fig. 2. –Variation of the population of the upper level $2p^5 3d(^1P_1)$ of the 15.02 Å resonance line, with increasing column density of Fe XVII; T_e=4 MK, for the three indicated electron densities.

Fig. 3. Column density dependence of the photon flux ratios of the 13.82, 15.02, 15.25, 15.45, 16.78, and 17.05 Å relative to the 17.10 Å line, calculated in cylindrical geometry, for T_e = 4 MK and $N_e = 10^{11}\ cm^{-3}$. Each of these resonance lines shows an initial increase relative to the dipole-forbidden 17.10 Å reference line which itself is found to be insensitive to opacity. The curves are plotted log-log to display the behavior of all of the line ratios on the same plot; however, this makes the peaks less apparent than in a semi-log plot (such as used in Fig. 4). Note that the intensity of 16.78 Å line, used as the reference line in Fig. 4, begins to rise significantly at an Fe XVII column density of about 10^{15} cm^{-2}.

Fig. 4.–(a) Column density dependence of the 15.02 resonance line photon flux relative to the flux of the 16.78 Å line, calculated in slab and cylindrical geometries; T_e=4 MK and N_e=10^{11} cm^{-3}. The line-center optical thicknesses involved are included as dashed curves (*right-hand scale*). A strong initial increase with increasing column density is seen to be present, somewhat less prominent in cylindrical geometry. (b) As for (a), but for the 15.26 line Å line. An initial increase with optical thickness is again present. (c) As for (a), but for the 15.45 Å line. The flux of this line relative to the 16.78 Å is seen to decrease monotonically with increasing column density.

Fig. 5 – Measured and calculated values of photon flux ratio F(15.02)/F(15.26) plotted vs. T_e. The crosses show SMM/FCS values with 1-σ errors for 31 active region spectra considered by Schmelz et al. 1996 and Saba et al. 1999. The FCS ratio for another active region spectrum studied by Waljeski et al. 1994 is shown as a diamond, also with 1-σ error. Ratios for the star Capella from Brinkman et al. 2000 and Canizares et al. 2000 are shown as asterisks. Laboratory measurements from EBIT experiments are plotted at temperatures corresponding to the respective beam energies: LLNL measurements (Brown et al. 1998) are shown as bold crosses; NIST measurements (Laming et al. 2000) are shown as triangles. The solid curve gives the present optically thin theoretical calculation of the ratio as a function of T_e; the dashed curve shows 0.75 of the theoretical values, consistent with the 25% estimated theoretical uncertainty.

Fig. 6 – "Theory normalized ratio" 15.02/15.26 vs. angle θ from disk center. Observed FCS values for the F(15.02)/F(15.26) photon ratio from Fig. 5, divided by current theory values for the respective temperatures (measured by Schmelz et al. 1996) and plotted vs. θ, with 0° corresponding to disk center and 90° to the limb. A value of unity for the "theory normalized ratio" would mean that the measured ratio matches the present theoretically optically thin value. The mean ratio $\simeq$ 0.55, indicating the observed ratios are about half of that predicted.

Fig. 7 – Measured and calculated values of various Fe XVII photon flux ratios plotted vs. T_e. For each ratio, the observed FCS values (for the same spectra as used in Figs. 5 and 6) are shown as crosses; the Capella ratio from Canizares et al. 2000 is shown as an asterisk; the NIST EBIT measurements are shown as triangles at temperatures corresponding to the respective beam energies; the solid curve gives the present optically thin theoretical calculation as a function of T_e; the dashed curve is 0.75 or 1.33 times the theoretical curve, corresponding roughly to the expected theoretical uncertainty, for comparison with the measurements. The 12 panels show the behaviors for the flux ratios: (a) F(15.02)/F(16.78), (b) F(15.26)/F(16.78), (c) F(17.05)/F(16.78), (d) F(15.02)/F(17.05), (e) F(15.26)/F(17.05), (f) F(17.10)/F(17.05), (g) F(15.02)/F(17.10), (h)

F(15.26)/F(17.10), (i) F(16.78)/F(17.10), (j) F(15.02)/F(17.05 + 17.10), (k) F(15.26)/F(17.05 + 17.10), and (l) F(15.26)/F(17.05 + 17.10). The last three panels are included to allow comparison with the NIST EBIT measurements, in which the 17.05 Å and 17.10 Å lines were not resolved.

Fig. 8 – Various "theory normalized" FCS ratios vs. angle θ from disk center. The ratios shown in the nine panels here – (a) 15.02/16.78, (b) 15.26/16.78, (c) 17.05/16.78, (d) 15.02/17.05, (e) 15.26/17.05, (f) 17.10/17.05, (g) 15.02/17.10, (h) 15.26/17.10, (i) 16.78/17.10 – correspond to the (unnormalized) FCS measured values for the photon flux ratios in the first nine panels in Fig. 7, each divided by the current theory ratios (evaluated at the temperatures measured by Schmelz et al. 1996) and then plotted vs. θ.

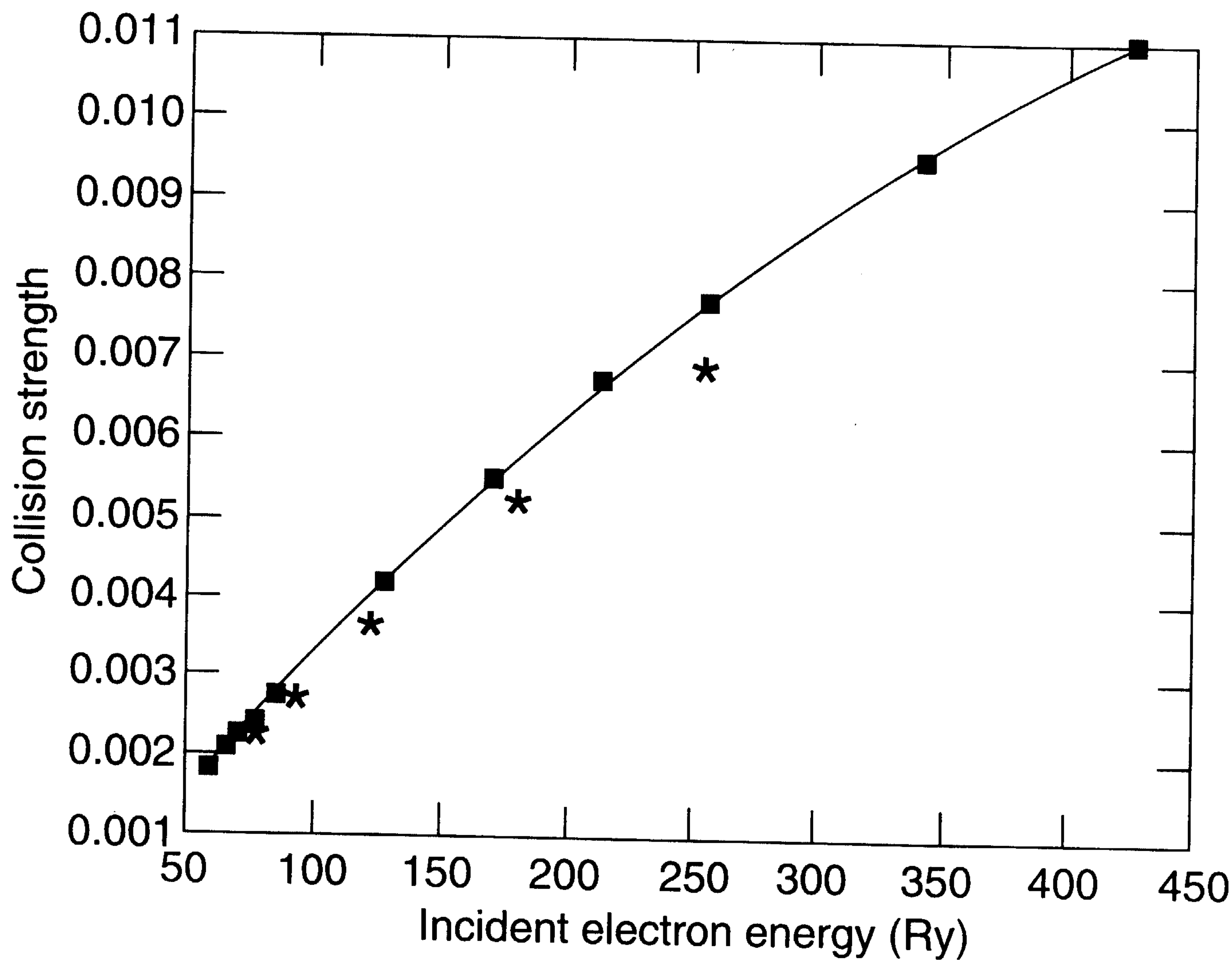
Collision strength
0.011
0.010
0.009
0.008
0.007
0.006
0.005
0.004
0.003
0.002
0.001
50
100
150
200
250
300
350
400
450
Incident electron energy (Ry)

B179.001

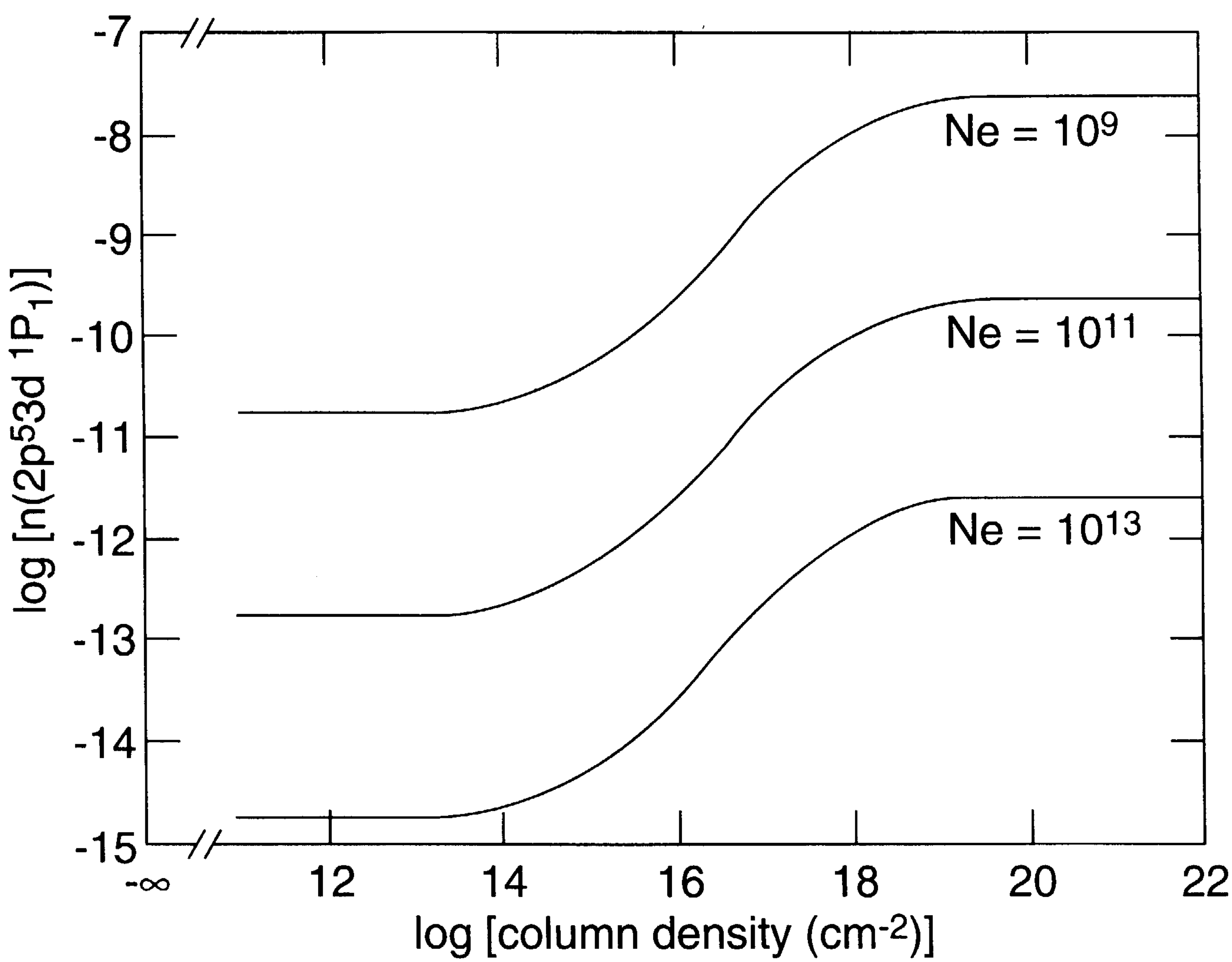
log [n(2p53d 1P1)]
-7
-8
-9
-10
-11
-12
-13
-14
-15
-∞
12
14
16
18
20
22
log [column density (cm-2)]
Ne = 109
Ne = 1011
Ne = 1013

C179.001

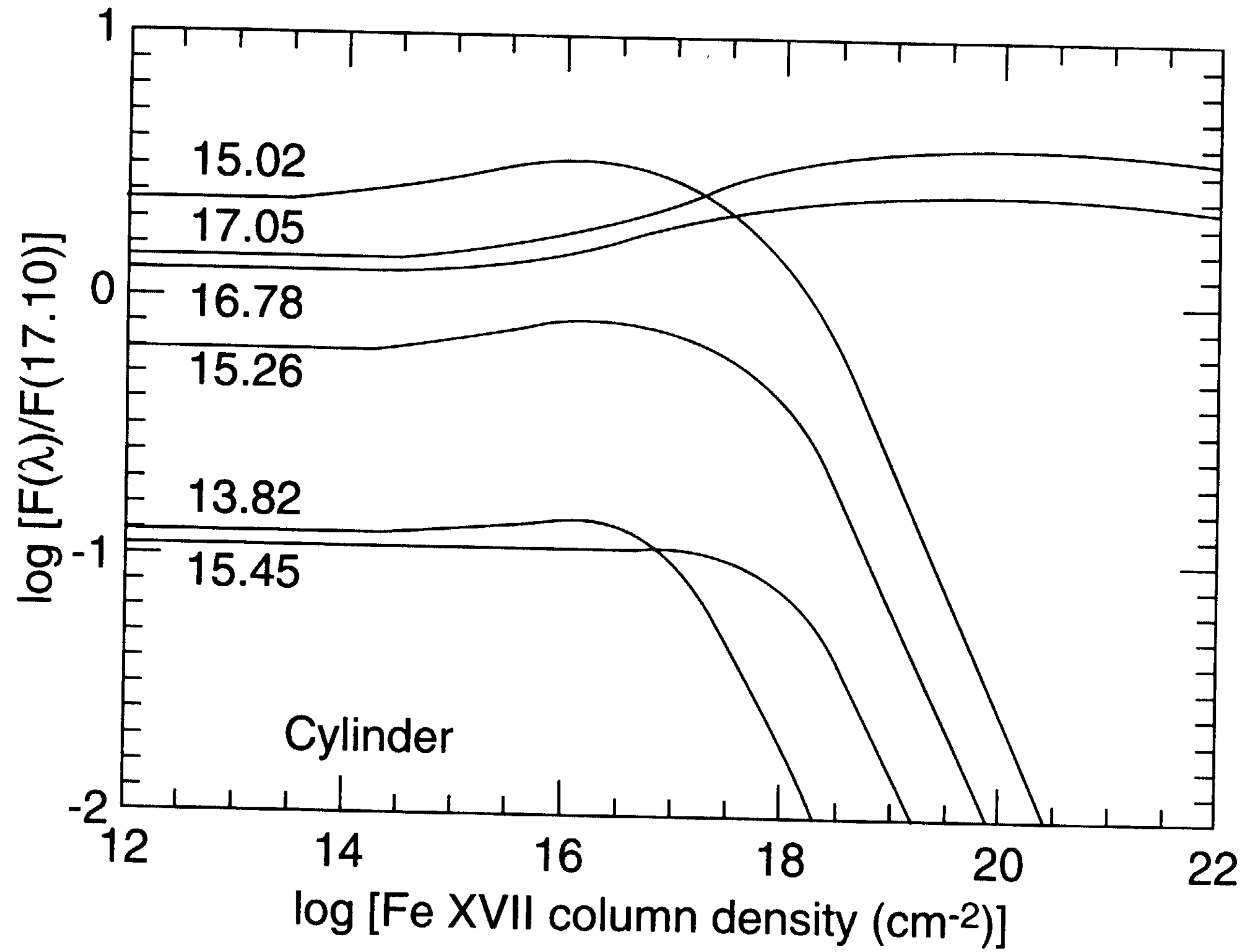
1
0
-1
-2
12
14
16
18
20
22
15.02
17.05
16.78
15.26
13.82
15.45
Cylinder
log [F(λ)/F(17.10)]
log [Fe XVII column density (cm-2)]

C179.005

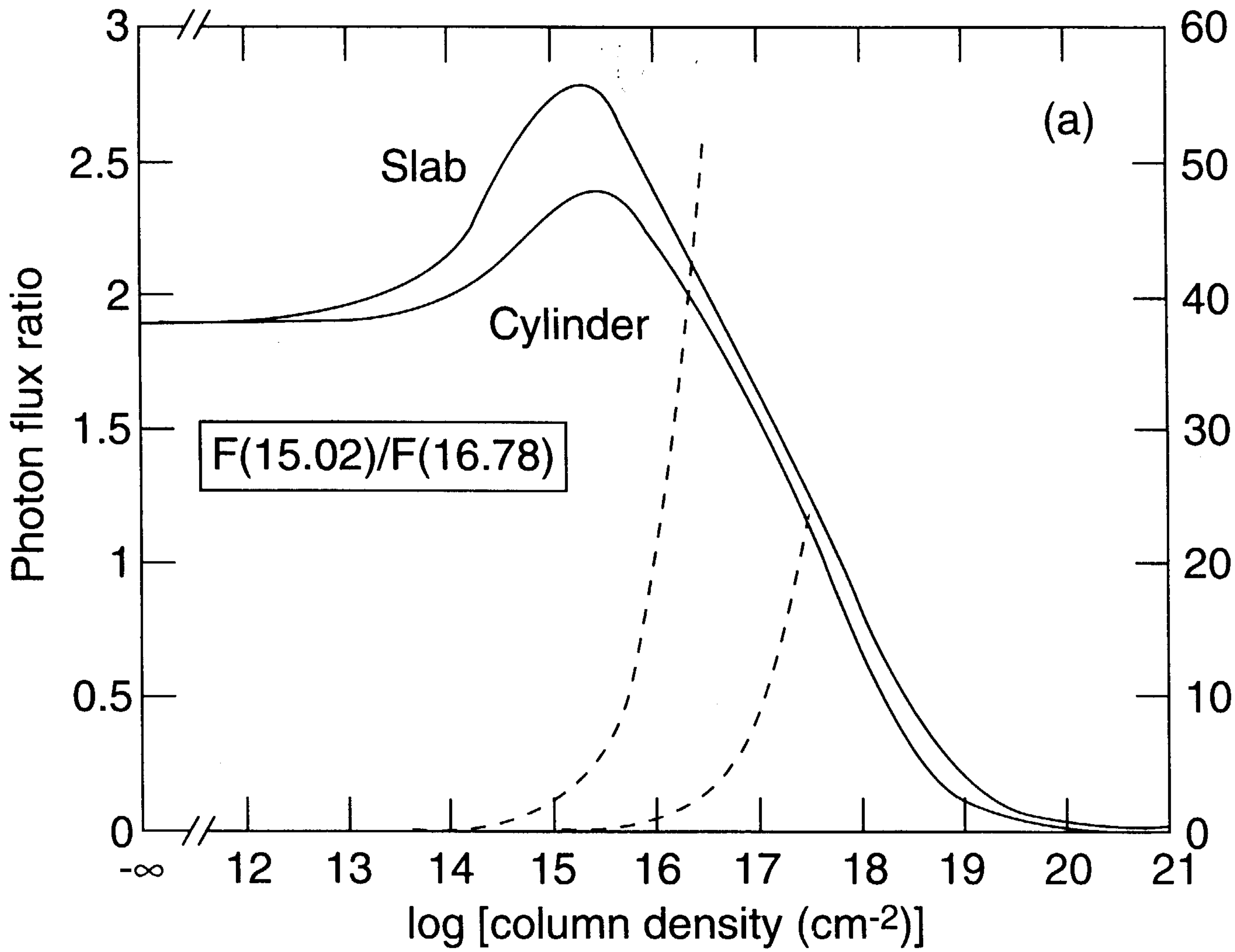
(a)
Slab
Cylinder
F(15.02)/F(16.78)
Photon flux ratio
log [column density (cm-2)]
3
2.5
2
1.5
1
0.5
0
60
50
40
30
20
10
0
-∞
12
13
14
15
16
17
18
19
20
21

C179.002

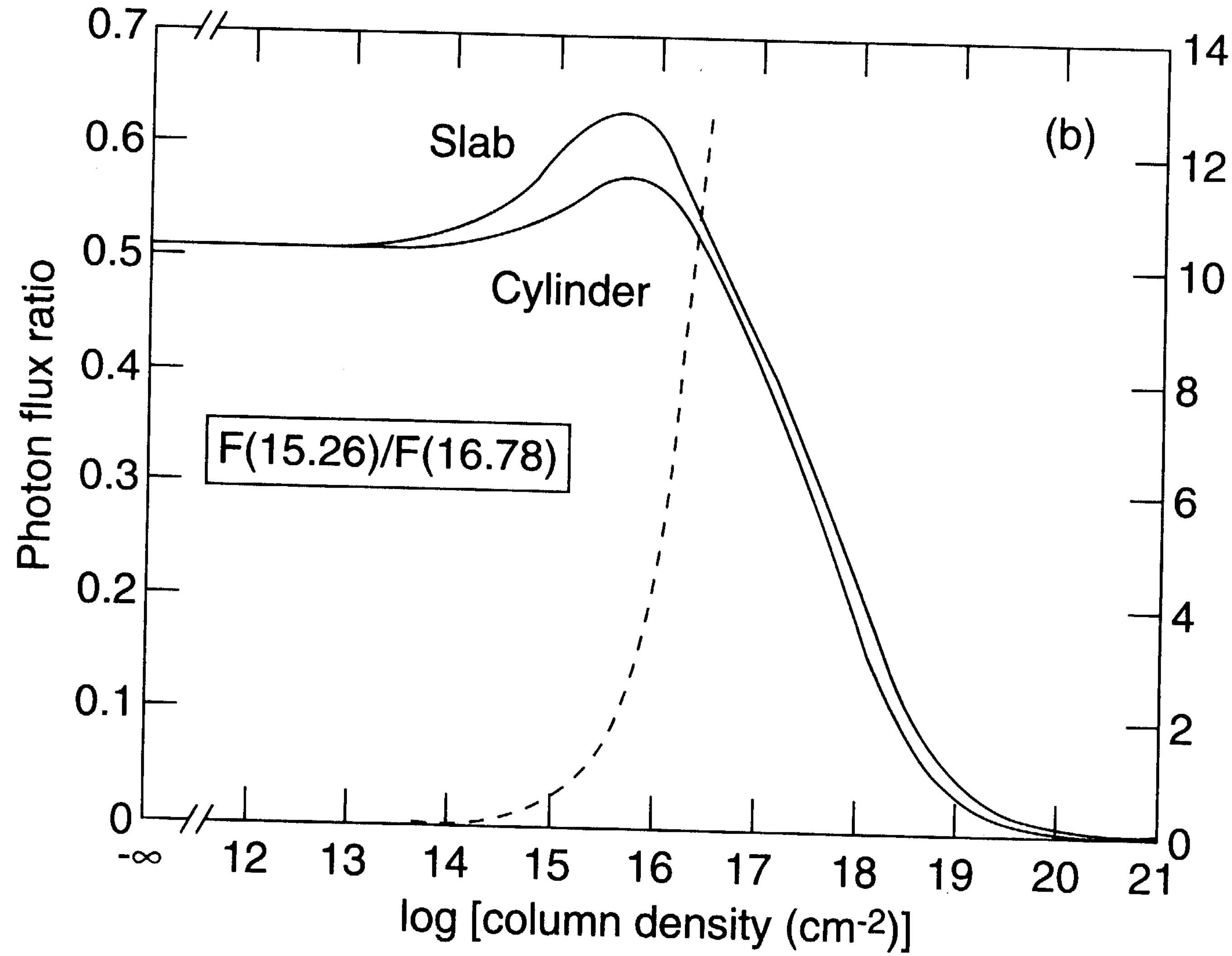

Photon flux ratio
0.7
0.6
0.5
0.4
0.3
0.2
0.1
0
-∞
12
13
14
15
16
17
18
19
20
21
14
12
10
8
6
4
2
0
Slab
Cylinder
(b)
F(15.26)/F(16.78)
log [column density (cm-2)]

C179.003

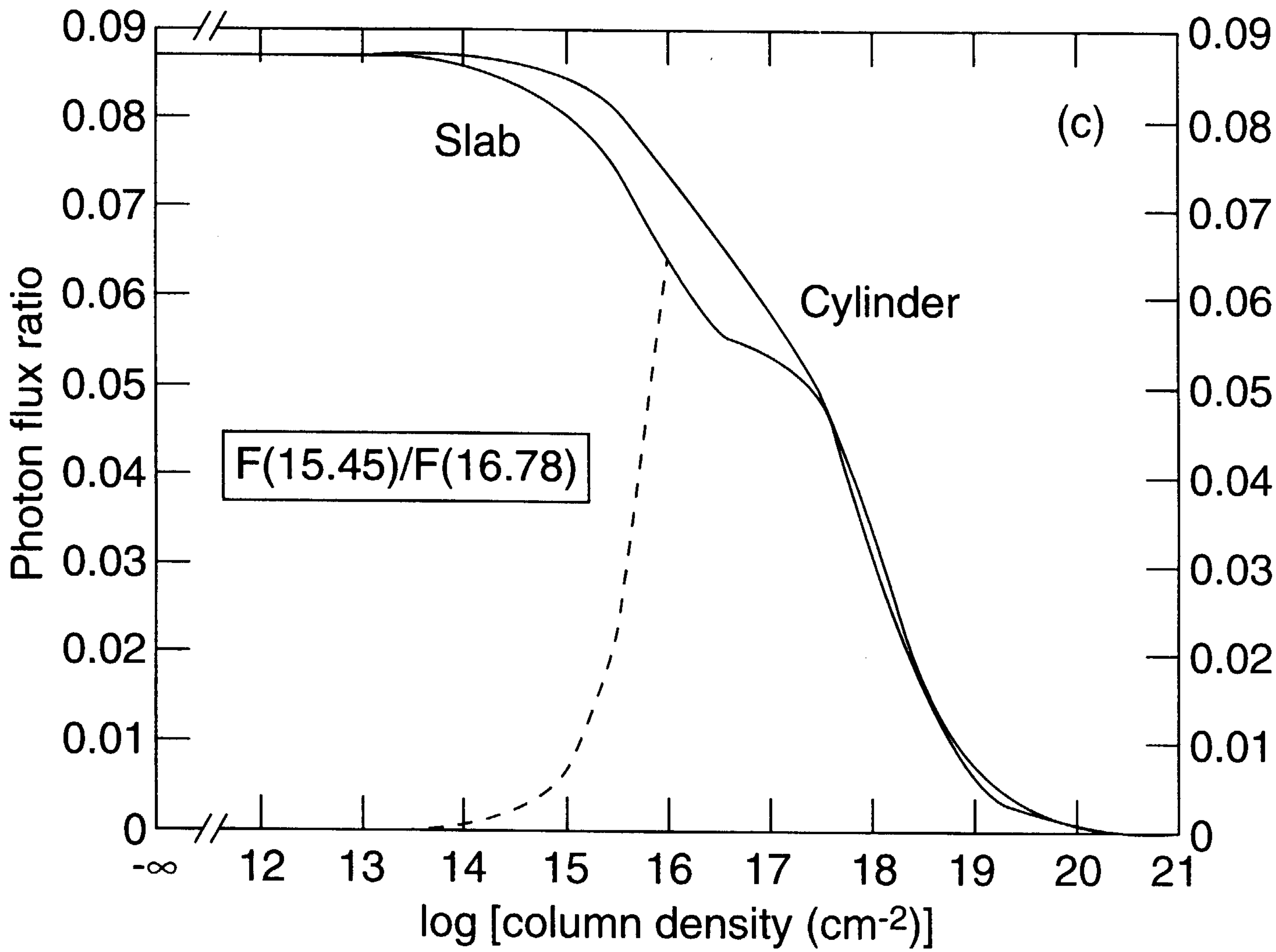
Photon flux ratio
0.09
0.08
0.07
0.06
0.05
0.04
0.03
0.02
0.01
0
-∞
12
13
14
15
16
17
18
19
20
21
log [column density (cm-2)]
Slab
Cylinder
(c)
F(15.45)/F(16.78)

C179.004

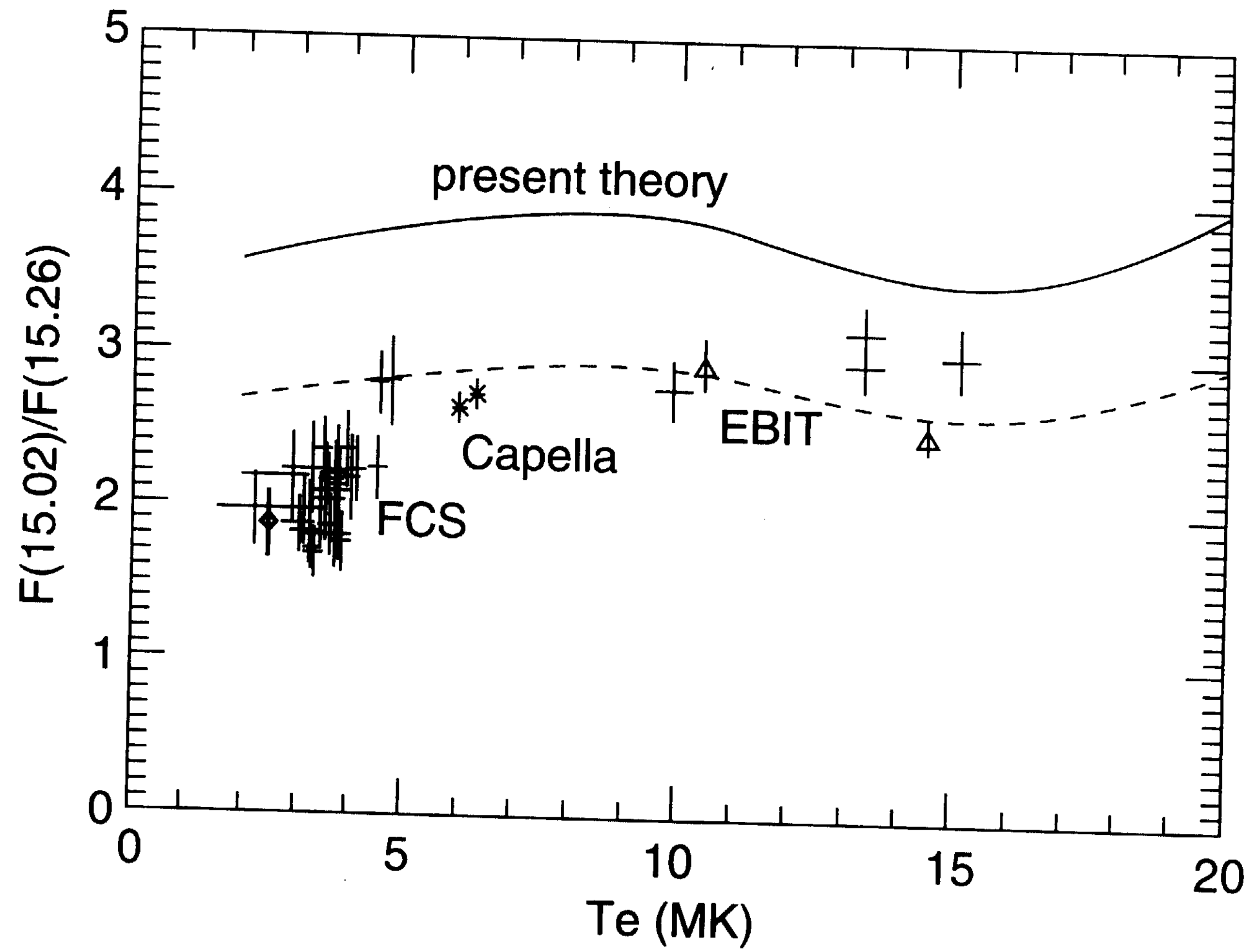
present theory
Capella
EBIT
FCS
F(15.02)/F(15.26)
Te (MK)
0
1
2
3
4
5
0
5
10
15
20

C179.006

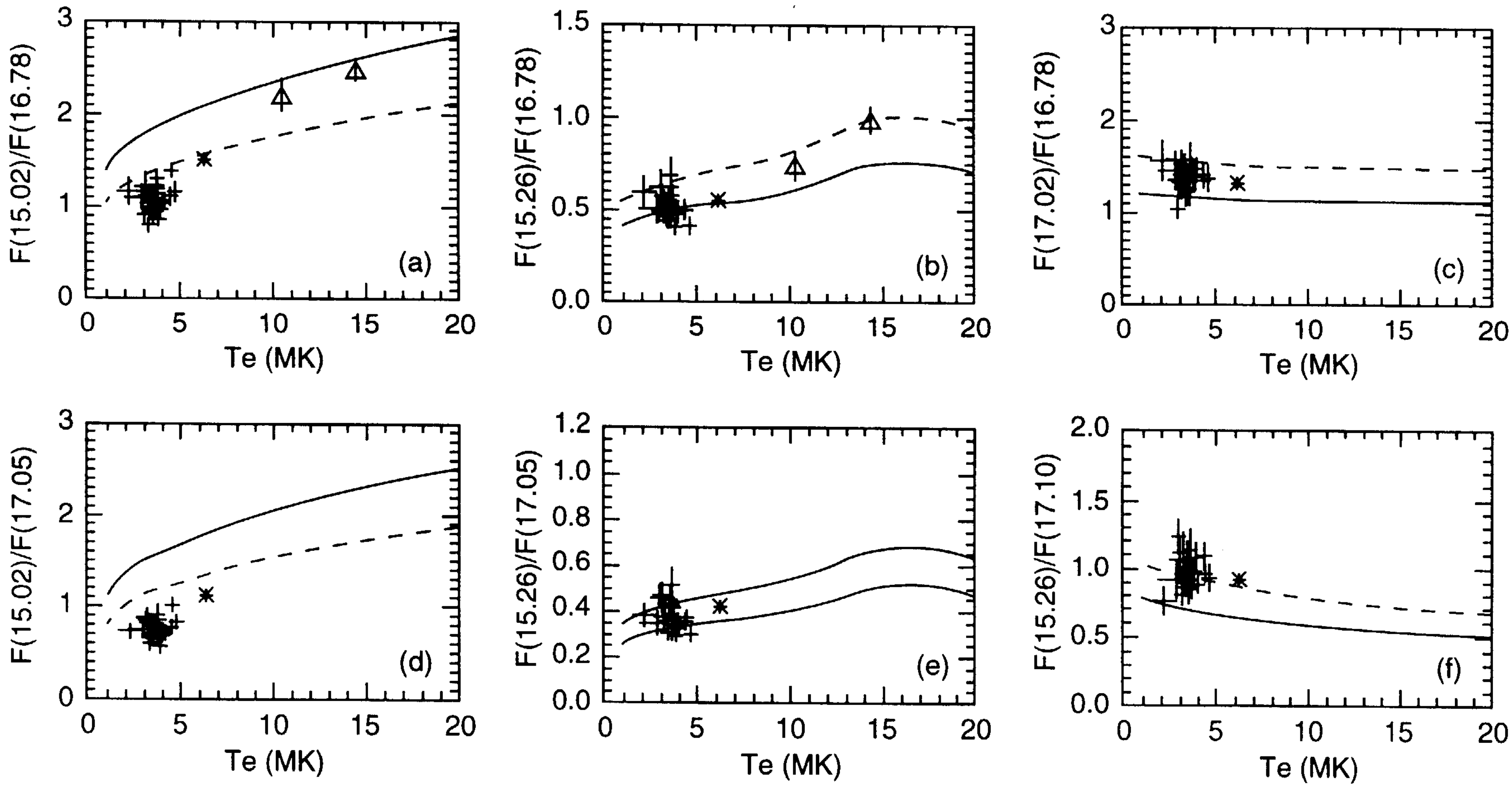
F(15.02)/F(16.78)
F(15.26)/F(16.78)
F(17.02)/F(16.78)
F(15.02)/F(17.05)
F(15.26)/F(17.05)
F(15.26)/F(17.10)
Te (MK)
(a)
(b)
(c)
(d)
(e)
(f)

C179.008

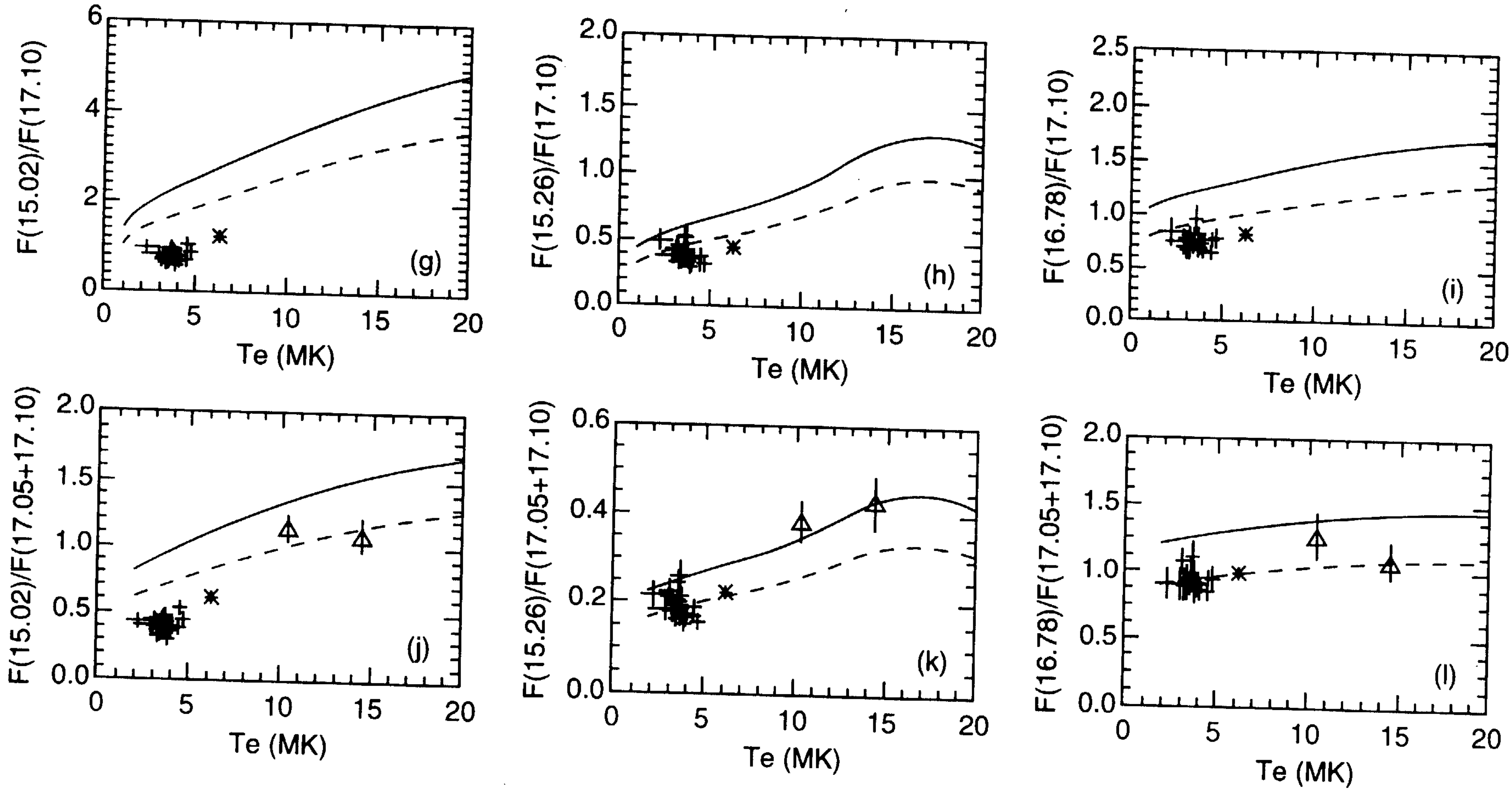
F(15.02)/F(17.10)
(g)
F(15.26)/F(17.10)
(h)
F(16.78)/F(17.10)
(i)
F(15.02)/F(17.05+17.10)
(j)
F(15.26)/F(17.05+17.10)
(k)
F(16.78)/F(17.05+17.10)
(l)
Te (MK)

C179.009

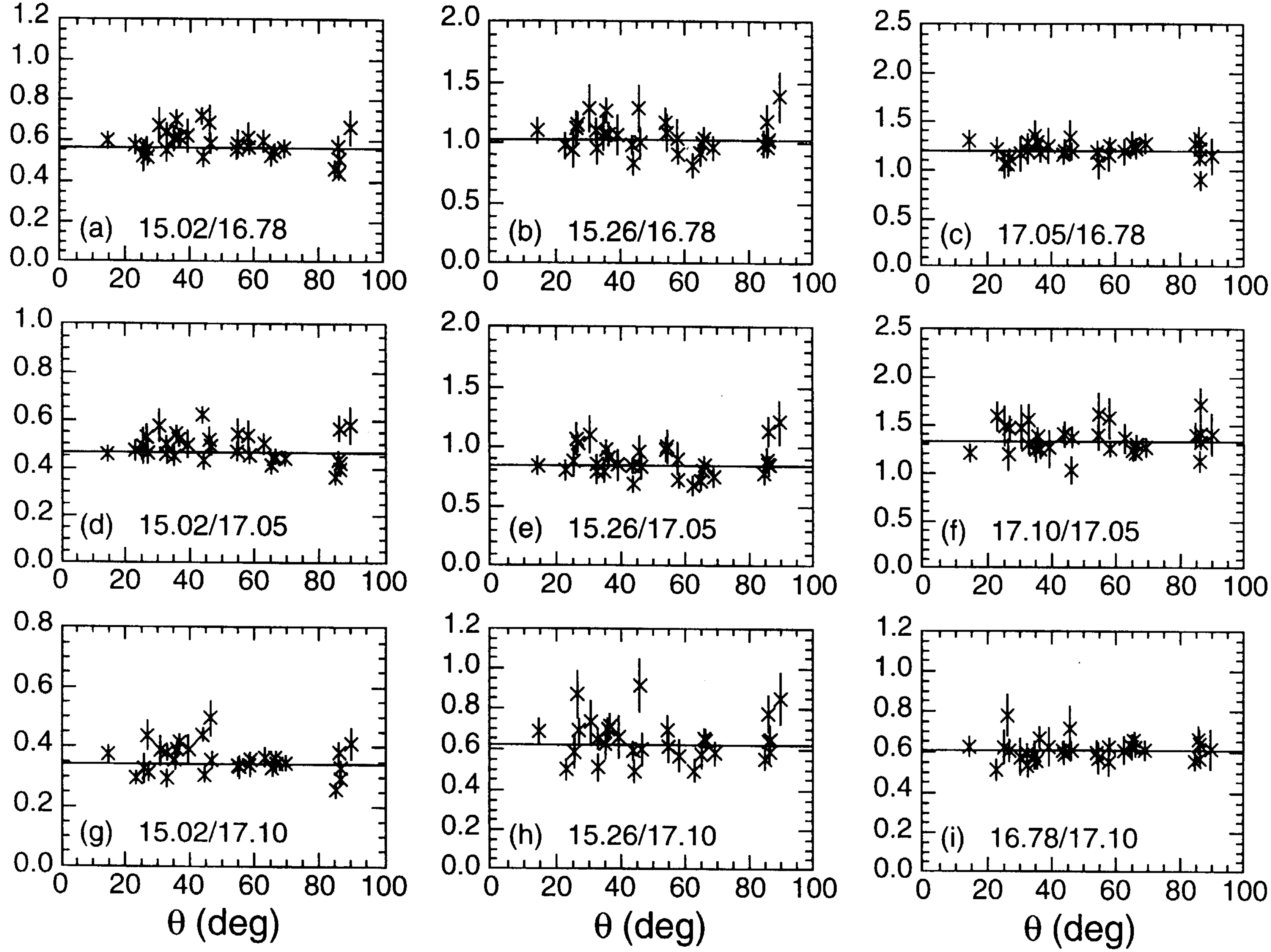
(a) 15.02/16.78
(b) 15.26/16.78
(c) 17.05/16.78
(d) 15.02/17.05
(e) 15.26/17.05
(f) 17.10/17.05
(g) 15.02/17.10
(h) 15.26/17.10
(i) 16.78/17.10
θ (deg)
θ (deg)
θ (deg)

C179.010